Optimising NMR Spectroscopy through Method and Software Development

Jonathan Yong

University of Oxford

Contents

refsection:1

refsection:2

Chapter 2

Pure shift NMR

Pure shift NMR refers to the technique of acquiring NMR spectra free of multiplet structure, such that every chemical environment gives rise to a singlet.[1,2] In the context of this thesis, I use the term 'pure shift' exclusively to refer to broadband homodecoupled ^{1}H spectra. Here, 'broadband' means that the couplings are removed from the *entire spectrum*, as opposed to just a specific region (which thus excludes band-selective refocusing techniques). 'Homodecoupled' refers to the removal of *homonuclear* couplings: unlike heteronuclear decoupling, this cannot be done during the acquisition period as the application of RF pulses will destroy the desired signal itself. Finally, although pure shift techniques can be applied to any nuclide, ^{1}H spectra are of greatest interest because of two factors: firstly, the narrow chemical shift range of ^{1}H which often leads to peak overlap; and secondly, the abundance of ^{1}H–^{1}H couplings in typical organic molecules.

In the first two sections, I first cover the theory underpinning, and a brief history of, pure shift experiments. I then describe my work towards increasing the quality of pure shift experiments: this is measured both in terms of *sensitivity* as well as *purity*, i.e. the lack of spectral artefacts arising from imperfect decoupling. Each of the approaches described here is compared against the PSYCHE pure shift method, which is the current state of the art. Finally, I end with a section discussing the combination of pure shift diffusion spectroscopy—formally a pseudo-3D experiment—with the use of ultrafast NMR techniques to collapse the diffusion dimension. This last project was carried out in collaboration with Jean-Nicolas Dumez (University of Nantes).

The work in this chapter has not been submitted for publication.

2.1 Theoretical background

In chapter 1, I showed how density operators could be expressed in either of the two bases $\{E, I_x, I_y, I_z\}$ or $\{E, I_z, I_+, I_-\}$, depending on which was most mathematically expedient. To analyse pure shift NMR, it turns out to be most convenient to introduce a third basis, namely $\{I_\alpha, I_\beta, I_+, I_-\}$.[3–5] The definitions of these terms are given in eq. (1.6): it is clear from there that, when expressed in the Zeeman basis, each matrix element of the density operator corresponds to one of these terms:

$$\rho = \begin{pmatrix} \rho_\alpha & \rho_+ \\ \rho_- & \rho_\beta \end{pmatrix} = \rho_\alpha I_\alpha + \rho_+ I_+ + \rho_- I_- + \rho_\beta I_\beta. \tag{2.1}$$

{eq:single_element_ope

In systems containing multiple spins, the corresponding *single-element operators* are just the products of these operators. In this section, I use a system with two weakly coupled spins I_1 and I_2 to illustrate the ideas behind pure shift NMR. We have that $H_{\text{free},I} = \Omega_1 I_{1z} + \Omega_2 I_{2z} + 2\pi J I_{1z} I_{2z}$, which is diagonal in the Zeeman basis:

$$H_{\text{free}} = \begin{pmatrix} \omega_{\alpha\alpha} & 0 & 0 & 0 \\ 0 & \omega_{\alpha\beta} & 0 & 0 \\ 0 & 0 & \omega_{\beta\alpha} & 0 \\ 0 & 0 & 0 & \omega_{\beta\beta} \end{pmatrix}. \tag{2.2}$$

{eq:h_free_weak}

Here, $\omega_{\lambda\mu} = \langle\lambda\mu|H_{\text{free},I}|\lambda\mu\rangle$ $(\lambda, \mu \in \{\alpha, \beta\})$ represents the precession frequency of the state $|\lambda\mu\rangle$. Given that $I_z|\alpha\rangle = (1/2)|\alpha\rangle$ and $I_z|\beta\rangle = -(1/2)|\beta\rangle$, these frequencies are relatively easy to work out:

$$\omega_{\alpha\alpha} = \frac{1}{2}(\Omega_1 + \Omega_2 + \pi J), \quad \omega_{\alpha\beta} = \frac{1}{2}(\Omega_1 - \Omega_2 - \pi J),$$
$$\omega_{\beta\alpha} = \frac{1}{2}(-\Omega_1 + \Omega_2 - \pi J), \quad \omega_{\beta\beta} = \frac{1}{2}(-\Omega_1 - \Omega_2 + \pi J). \tag{2.3}$$

{eq:state_precessions}

The corresponding propagator $U(\tau) = \exp(-iH_{\text{free},I}\tau)$ is then just:

$$U(\tau) = \begin{pmatrix} \exp(-i\omega_{\alpha\alpha}\tau) & 0 & 0 & 0 \\ 0 & \exp(-i\omega_{\alpha\beta}\tau) & 0 & 0 \\ 0 & 0 & \exp(-i\omega_{\beta\alpha}\tau) & 0 \\ 0 & 0 & 0 & \exp(-i\omega_{\beta\beta}\tau) \end{pmatrix}. \tag{2.4}$$

{eq:u_free_weak}

Consequently, the evolution of the single-element operators under $H_{\text{free},I}$ is extraordinarily simple to calculate in matrix form: for example, we have that

$$I_{1+}I_{2\alpha} = \begin{pmatrix} 0 & 0 & 1 & 0 \\ 0 & 0 & 0 & 0 \\ 0 & 0 & 0 & 0 \\ 0 & 0 & 0 & 0 \end{pmatrix}, \tag{2.5}$$

{eq:single_elem_plusal

so $U(\tau)I_{1+}I_{2\alpha}U^\dagger(\tau)$ is

$$\begin{pmatrix} 0 & 0 & \exp(-i\omega_{\alpha\alpha}\tau)\exp(i\omega_{\beta\alpha}\tau) & 0 \\ 0 & 0 & 0 & 0 \\ 0 & 0 & 0 & 0 \\ 0 & 0 & 0 & 0 \end{pmatrix} = \exp[-i(\Omega_1 + \pi J)\tau]I_{1+}I_{2\alpha}. \qquad (2.6)$$

{eq:single_elem_plusal

Essentially, under $H_{\text{free},I}$, all of these operators acquire phase factors which depend on the difference between two of the frequencies $\omega_{\lambda\mu}$. I explicitly state the rules for the single-quantum operators on spin 1 here:[*]

$$I_{1+}I_{2\alpha} \longrightarrow \exp[-i(\Omega_1 + \pi J)\tau]I_{1+}I_{2\alpha} \qquad (2.7)$$

{eq:shift_basis_evolut

$$I_{1+}I_{2\beta} \longrightarrow \exp[-i(\Omega_1 - \pi J)\tau]I_{1+}I_{2\beta} \qquad (2.8)$$

{eq:shift_basis_evolut

$$I_{1-}I_{2\alpha} \longrightarrow \exp[i(\Omega_1 + \pi J)\tau]I_{1-}I_{2\alpha} \qquad (2.9)$$

{eq:shift_basis_evolut

$$I_{1-}I_{2\beta} \longrightarrow \exp[i(\Omega_1 - \pi J)\tau]I_{1-}I_{2\beta} \qquad (2.10)$$

{eq:shift_basis_evolut

The rules for the corresponding operators on spin 2 can be easily obtained by permutation of labels. Notice that the evolution frequencies of the -1-quantum operators (eqs. (2.9) and (2.10)) each correspond to one peak of the corresponding multiplet in an NMR spectrum: for example, $\Omega_1 + \pi J$ and $\Omega_1 - \pi J$ correspond to the two peaks of the spin-1 doublet.

Consider now a simple spin echo sequence: $90°_x–\tau–180°_x–\tau–$detection. The initial excitation pulse acts on both spins 1 and 2, and thus generates a mixture of all eight possible single-quantum operators (the four above plus four more on spin 2). For simplicity, we consider only the $I_{1+}I_{2\alpha}$ term. This evolves in the first τ delay to give $\exp[-i(\Omega_1 + \pi J)\tau]I_{1+}I_{2\alpha}$. The 180° pulse *flips* both spins 1 and 2, in that it causes the transitions $I_+ \leftrightarrow I_-$ and $I_\alpha \leftrightarrow I_\beta$; consequently, we have that

$$\exp[-i(\Omega_1 + \pi J)\tau]I_{1+}I_{2\alpha} \longrightarrow \exp[-i(\Omega_1 + \pi J)\tau]I_{1-}I_{2\beta}. \qquad (2.11)$$

{eq:spin_echo_1}

In the second delay, we get a second phase factor from the evolution of the $I_{1-}I_{2\beta}$ operator:

$$\exp[-i(\Omega_1 + \pi J)\tau]I_{1-}I_{2\beta} \longrightarrow \exp[-i(\Omega_1 + \pi J)\tau]\exp[i(\Omega_1 - \pi J)\tau]I_{1-}I_{2\beta}$$

$$= \exp(-2i\pi J\tau)I_{1-}I_{2\beta}. \qquad (2.12)$$

{eq:spin_echo_2}

Detection of this gives us one of the two peaks of the spin-1 doublet, as described previously, but with a phase factor tacked on. The Ω_1 terms in the phase factor are cancelled out, which reflects the fact that the offset (or chemical shift) is refocused by the 180° pulse. However, the J-evolution is not refocused, which leads to characteristic phase distortions in the detected multiplets. The

---

[*]Note that § 10.4.2 of Keeler's text[3] has a sign error in these equations—the sign of the πJ evolution is flipped—though it proves to be inconsequential as the sign of J cannot be observed.

same is true of the seven other single-quantum operators.

In order to refocus the J-evolution as well as the chemical shift, we would need—instead of a 180°
pulse—a pulse sequence element which simultaneously effects *all* of the following transitions on
spin 1:

$$I_{1+}I_{2\alpha} \longrightarrow I_{1-}I_{2\alpha}; \quad I_{1+}I_{2\beta} \longrightarrow I_{1-}I_{2\beta}; \quad I_{1-}I_{2\alpha} \longrightarrow I_{1+}I_{2\alpha}; \quad I_{1-}I_{2\beta} \longrightarrow I_{1+}I_{2\beta}; \tag{2.13}$$

{eq:pure_shift_require

and on spin 2:

$$I_{1\alpha}I_{2+} \longrightarrow I_{1\alpha}I_{2-}; \quad I_{1\beta}I_{2+} \longrightarrow I_{1\beta}I_{2+}; \quad I_{1\alpha}I_{2-} \longrightarrow I_{1\alpha}I_{2+}; \quad I_{1\beta}I_{2-} \longrightarrow I_{1\beta}I_{2-}. \tag{2.14}$$

{eq:pure_shift_require

Such an element forms the basis of a pure shift technique, and I refer to it here as a *pure shift
element* (PSE). The difficulty in designing a PSE is that *all* spins must be simultaneously decoupled
from each other (and not just one spin). For example, if we only had to invert spin 1 and not
spin 2 (i.e. only eq. (2.13) and not eq. (2.14)), this could be trivially accomplished by a selective
180° pulse on spin 1. However, this would not bring about the correct transitions for spin 2. Yet
another complicating factor is that the spins will have offsets and couplings which are *a priori*
not known; so the design of the PSE cannot use these parameters as inputs. These limitations
mean that it is impossible to accomplish the above transitions *in full*; rather, a more realistic
scenario involves

$$I_{1+}I_{2\alpha} \longrightarrow cI_{1-}I_{2\alpha} + \sum_i c_i' M_i \tag{2.15}$$

{eq:realistic_pse}

and likewise for the other operators. Here, the desired transition probability $c < 1$ directly
correlates with the sensitivity of the PSE, and the $M_i's$ are some other undesired operators which
(if detectable) lead to artefacts if not suppressed.

In the above discussion, note that the role of the PSE is to invert the I_+ and I_- terms, and to leave
the I_α and I_β terms untouched. The spins with I_+ and I_- terms are referred to as *active spins*,
and the I_α and I_β spins as *passive spins*. Thus, for example, in the context of eq. (2.13), spin 1
is active and spin 2 is passive. The detected signal always arises from the active spins (unless
coherence transfer between spins occurs, for example in the mixing period of a 2D pure shift
experiment).

Figure 2.1: Pulse sequence for the J-resolved (2DJ) experiment.

Before moving on to the discussion of how PSEs are implemented in practice, I insert a slight
digression about *J-resolved* (or *2DJ*) *spectroscopy*, which is very closely related to pure shift NMR.
The basic 2DJ sequence involves a spin echo of duration t_1, immediately followed by detection

(fig. 2.1). If we only consider a single operator and reuse the analysis above, setting the spin echo delay τ to be $t_1/2$ instead, then we have that

$$I_{1+}I_{2\alpha} \xrightarrow{t_1/2} \xrightarrow{180°} \xrightarrow{t_1/2} \exp(-i\pi Jt_1)I_{1-}I_{2\beta}. \tag{2.16}$$

{eq:2dj_operator_analy

This yields a complex signal of the form

$$s(t_1, t_2) = \exp(-i\pi Jt_1)\exp[i(\Omega_1 - \pi J)t_2], \tag{2.17}$$

{eq:2dj_signal}

which when Fourier transformed yields a phase twist lineshape at $(-\pi J, \Omega_1 - \pi J)$. The other component on spin 1 (starting from $I_{1+}I_{2\beta}$) likewise yields a phase twist at $(\pi J, \Omega_1 + \pi J)$. It has long been known that *shearing* this 2DJ spectrum by 45° (i.e. moving each data point (Ω_1, Ω_2) to $(\Omega_1, \Omega_2 - \Omega_1)$) generates a spectrum which only has chemical shift information in the ω_2 dimension. After magnitude-mode processing, projection of this spectrum onto the ω_2 axis, for example, would in principle yield a pure shift spectrum.[*] This is true, but in practice the phase twist lineshapes cause the resulting resolution to be very poor, which defeats the purpose of using a pure shift spectrum. To circumvent this issue, a number of special processing techniques have been proposed[7–9] (see also references therein); but more ideally, we want a phase-sensitive 2DJ spectrum, which can be obtained by recording a pair of 'echo' and 'antiecho' signals:[†]

$$s_{\text{echo}}(t_1, t_2) = \exp(i\pi Jt_1)\exp[i(\Omega_1 - \pi J)t_2] \tag{2.18}$$

{eq:2dj_signal_echo}

$$s_{\text{antiecho}}(t_1, t_2) = \exp(-i\pi Jt_1)\exp[i(\Omega_1 - \pi J)t_2] \tag{2.19}$$

{eq:2dj_signal_antiech

These can be processed in the same way as described in § 1.4.3 to yield double absorption-mode lineshapes. The antiecho signal (eq. (2.19)) is of course the same as in eq. (2.17), but to obtain the echo signal in eq. (2.18), we require a different pulse sequence with a PSE inserted just prior to detection:

$$I_{1-}I_{2\alpha} \xrightarrow{t_1/2} \exp[i(\Omega_1 + \pi J)t_1/2]I_{1-}I_{2\alpha} \tag{2.20}$$

{eq:2dj_signal_echo_ct

$$\xrightarrow{180°} \exp[i(\Omega_1 + \pi J)t_1/2]I_{1+}I_{2\beta} \tag{2.21}$$

$$\xrightarrow{t_1/2} \exp(i\pi Jt_1)I_{1+}I_{2\beta} \tag{2.22}$$

$$\xrightarrow{\text{PSE}} c\exp(i\pi Jt_1)I_{1-}I_{2\beta} \tag{2.23}$$

$$\xrightarrow{t_2} c\exp(i\pi Jt_1)\exp[i(\Omega_1 - \pi J)t_2]. \tag{2.24}$$

---

[*]Or equivalently, projection of the unsheared spectrum along a 45° axis.[6]

[†]The terms 'echo' and 'antiecho' refer to the relative senses of the coherences evolving during t_1 and t_2: in the echo spectrum these have opposite signs, e.g. I_zS_+ and I_- in the HSQC, and in the antiecho spectrum they have the same sign. As pointed out by Pell and Keeler,[10] this is not really appropriate for the 2DJ experiment since each half of t_1 has a coherence with a different sense, but we will stick to this nomenclature as the underlying concept is very similar to that of echo–antiecho processing.

(Note that we began the analysis with a different operator here, $I_{1-}I_{2\alpha}$, in order to end up with the same $I_{1-}I_{2\beta}$ operator just before detection.) In order to apply echo–antiecho processing, the decrease in sensitivity by a factor of c must also be applied to the antiecho spectrum: this can be done by simply inserting the PSE immediately after the initial excitation pulse, which simply scales all operators down by c. Thus, we see that *exactly the same PSE* allows us to generate pure shift spectra as well as absorption-mode 2DJ spectra: this has been previously demonstrated using various PSEs.[10,11]

In fact, the same formalism can be used to describe a family of small flip angle COSY experiments, including ECOSY[5,12,13] and *z*-COSY;[14–16] these are also closely related to pure shift NMR. In particular, the anti *z*-COSY experiment is a precursor to PSYCHE, and is analysed in § 2.2.3. However, a full discussion of these is beyond the scope of this thesis.

2.2 Pure shift in practice

In the previous section, I described the underlying theory used for analysing PSEs and showed how such an element could be used to record absorption-mode 2DJ spectra. From this, one can obtain a pure shift spectrum through shearing and projection. However, this is only an *indirect* route to a pure shift spectrum. In this section, we will tackle the main question of how pure shift experiments may be *directly* acquired using a PSE. Following this, I cover several examples of PSEs reported in the literature. This is not an exhaustive survey of pure shift methods: I only choose to cover a handful of PSEs which specifically accomplish the transformations listed in eqs. (2.13) and (2.14). Thus, for example, constant-time techniques (which are widely used to suppress ^{13}C–^{13}C couplings in labelled biomolecules) are not mentioned.

2.2.1 Acquisition modes

Restating eq. (2.15), suppose we have a PSE which accomplishes the transformation

$$I_{1+}I_{2\alpha} \longrightarrow cI_{1-}I_{2\alpha} + \sum_i c_i' M_i. \qquad (2.25) \quad \text{\{eq:pse\_revisited\}}$$

The simplest method of using this is to insert it in the middle of a t_1 period of a 2D experiment. This is actually not entirely desirable, because the PSE causes *both* chemical shifts and J-couplings to be refocused; consequently, there will be *no* frequency modulation during t_1 at all! It is more sensible to combine the PSE with a hard 180° pulse, which refocuses only chemical shifts. Together, the effect is to refocus J-couplings and allow chemical shifts to evolve; this combination is thus called a *J-refocusing element*, or JRE (fig. 2.2a). We can equivalently say that the JRE flips all passive spins and leaves active spins untouched. This distinction between a JRE and a PSE is

./figures/pureshift/modes.png

Figure 2.2: Possible acquisition modes for pure shift spectroscopy. The red box labelled 'PSE' indicates a generic pure shift element, which can be any of those described in the main text. In practice, gradients are also used to suppress unwanted coherence transfers; these are not shown here for simplicity. **(a)** Insertion of a J-refocusing element (JRE) in the centre of an indirect-dimension evolution period, which leads to a spectrum which is pure shift in F_1. The 90°–τ_m–90° mixing period shown here is that of a NOESY experiment, but in principle it can be anything. **(b)** Real-time acquisition of a 1D pure shift spectrum in chunks of duration T_{chunk}. **(c)** Interferogram acquisition of a 1D pure shift spectrum, where t_1 is lengthened by T_{chunk} every increment.

important and will be referred to several times in this chapter.

Implementing a JRE in the middle of a t_1 period is simple, requiring minimal modification of existing 2D experiments. Furthermore, the pure shift 'character' of the F_1 dimension may then be mapped to the F_2 dimension through indirect covariance processing.[17–22] However, the increased resolution in the F_1 dimension provided by homodecoupling cannot really be reaped unless many t_1 increments are acquired. Furthermore, this does not help with acquiring a 1D pure shift spectrum, where there is no indirect dimension.

This brings us to the second acquisition mode for pure shift data, called *real-time acquisition.*[23–26] Here, JREs are inserted in the middle of an acquisition period at regular intervals, causing the chemical shift evolution to be effectively 'suspended' for the duration of the JRE, and the sense of J-evolution to be reversed (fig. 2.2b).* This leads to a series of FID 'chunks' which must then be concatenated to form the desired FID. To prevent the J-coupling from evolving too much during a single chunk, the required spacing of the JREs, or equivalently the duration of each chunk T_{chunk}, must satisfy $T_{chunk} \ll 1/J$ (in practice, it is on the order of $1/(2J)$). Naturally, real-time acquisition still comes with the sensitivity penalty of *c*. However, it allows a pure shift spectrum to be acquired in effectively the same time as the original coupled spectrum; its 'single-scan'

---

*Relaxation during the JRE must also be taken into account for the real-time method: this causes each successive chunk to decay in intensity faster than usual, thereby leading to peak broadening, which can be an issue for very long JREs. In contrast, the interferogram method as only one JRE is applied on each increment, so the losses due to relaxation during the JRE are simply a constant factor.

nature also allows, for example, the application of hyperpolarisation techniques which cannot be reproducibly repeated.[27,28]

Unfortunately, it is not always possible to perform real-time acquisition. The reason is because the JRE is applied multiple times, and each time it is, it must select for the same active and passive spins in the same molecule as it did the last time. In other words, *for any given molecule in the sample*, it must enforce this CTP:

$$I_{1-}I_{2\alpha} \xrightarrow{\text{JRE}} I_{1-}I_{2\beta} \xrightarrow{\text{JRE}} I_{1-}I_{2\alpha} \xrightarrow{\text{JRE}} I_{1-}I_{2\beta} \xrightarrow{\text{JRE}} \cdots \qquad (2.26)$$

As will be described later, the BIRD and Zangger–Sterk methods always select the same active spins in the same molecules, but the PSYCHE method does not. Therefore, in order to acquire pure shift PSYCHE spectra, we have to resort to the *interferogram method*, where each chunk is obtained as a separate increment of a 2D experiment (fig. 2.2c). The insertion of the JRE in the middle of the t_1 period means that when detection is started, it is 'as if' only the chemical shift has evolved for a period t_1. On each increment, one chunk—again of duration $T_{\text{chunk}} \ll 1/J$—is detected, and then t_1 is incremented by T_{chunk} so that the next chunk can be recorded. Finally, the chunks are stitched together to form the requisite FID.[*] Since the indirect dimension is not processed by a Fourier transform, this is sometimes called a *pseudo-2D* experiment (or *pseudo-3D* if this is applied to the direct dimension of a 2D experiment, and so on). In this case, the sensitivity drop c is incurred, but there is on top of that also a time penalty in that the experiment duration must be lengthened by n times in order to collect n chunks. n is typically on the order of 16–32.

2.2.2   Pure shift elements

Figure 2.3: A selection of pure shift elements. **(a)** Zangger–Sterk PSE,[31] involving the combination of a selective 180° refocusing pulse and a weak gradient. **(b)** BIRD PSE;[32,33] the delay Δ is set to $1/(4 \cdot {}^1J_{\text{CH}})$. **(c)** Time-reversal PSE,[13] simply consisting of a hard pulse with variable flip angle β. Multiple spectra with different values of β must be co-added to suppress artefacts (though not completely, as discussed in the text). **(d)** PSYCHE PSE,[34] consisting of two saltire pulses[35,36] with flip angle β, and a weak gradient.

---

[*]Not included in figs. 2.2b and 2.2c is the extra detail that scalar couplings are usually allowed to evolve for a period of $T_{\text{chunk}}/2$ at the start of the sequence by the addition of a spin echo: this amounts to a *prefocusing* of J-evolution, such that J-coupling is refocused in the middle of the chunk rather than the beginning.[29] This allows chunk sizes twice as large to be used, reducing the total duration of the experiment. This J-prefocusing can also be done in a more intelligent manner via the SAPPHIRE method,[30] which is discussed in more detail in § 4.3.6.

Zangger–Sterk

We are finally now in a position to study individual PSEs and their mechanisms of action. We begin with the Zangger–Sterk (ZS, or 'slice-selective') PSE,[31] in which a selective refocusing pulse and a weak gradient are simultaneously applied (fig. 2.3a). In practice, an rSNOB pulse[37] is often used as the refocusing pulse. The effect of the gradient is to make each spin in the sample have a spatially dependent offset; therefore, in each *slice* (or cross-section) of the sample, a different spin will fall within the specific bandwidth of the refocusing pulse. This spin is refocused by the PSE and therefore becomes the active spin *within that specific slice*; the bracketing pair of CTP gradients serve to destroy coherences on all the other spins which are not inverted. Each signal of the pure shift spectrum therefore derives from a specific slice of the sample; during direct detection, all slices simultaneously contribute to the signal, thus yielding a broadband pure shift spectrum.

The sensitivity of the ZS method tends to be low (the factor c tends to be on the order of ~ 0.01 to 0.05), as each signal only comes from a narrow section of the sample. Nevertheless, it still finds wide usage in pure shift applications nowadays, especially because it is compatible with the real-time acquisition mode:[24] as long as the pulse and the weak gradient are the same each time, then the same active spins will always be chosen in the same slice (as long as diffusion effects are ignored). The PSE can also be customised through the bandwidth of the refocusing pulse: decreasing this improves the spatial differentiation between spins which have similar intrinsic offsets, yielding better decoupling quality, albeit at the cost of sensitivity. The ZS element can be easily—and has been—adapted for use in many experiments, including (but not limited to) absorption-mode 2DJ spectroscopy[10] and selective refocusing (SERF) experiments for the measurement of $^{n}J_{\mathrm{HH}}$.[38–41]

BIRD

Next up is the *bilinear rotation decoupling* (BIRD) pulse element (fig. 2.3b). BIRD is not spatially selective like the ZS method; instead, it is *isotope-selective* in that it acts as a 180°_{y} pulse on ^{13}C–bound protons, and does not affect ^{12}C–bound protons. Consequently, all ^{13}C–bound protons become the active spins in the context of pure shift NMR. The first report of the BIRD element,[32] in 1982, was clearly ahead of its time: it reported the use of an interferogram-type approach to obtain 1D pure shift spectra. However, in the subsequent decades, this seemed to have been forgotten: BIRD found much more use as an isotope-selective rotation element in heteronuclear NMR,[42] until its use as a pure shift element was 'rediscovered'.[33,43]

An immediate drawback of BIRD is that it does not decouple geminal (diastereotopic) CH_2 groups, as both protons would be either both active or both passive. The sensitivity penalty of BIRD is also relatively severe: the factor c derives from the natural abundance of ^{13}C, which

is approximately 0.011. However, it is also compatible with real-time acquisition,[23] and has found particular success as a pure shift element in the F_2 dimension of HMQC and HSQC experiments:[26,43–47] in this case, the use of BIRD leads to no loss of sensitivity as only ^{13}C–bound protons are detected in HSQC experiments anyway.[*] It should be noted that the BIRD element does not need to be combined with a hard 180° pulse to form a JRE: the inverse effect of only flipping the passive spins can be accomplished by simply changing the phase of both internal 180° pulses to $+y$. Using the nomenclature of Uhrín et al.,[42] the PSE and JRE forms of the BIRD pulse can be labelled as BIRD^{d,X} and BIRD^{r,X} respectively.

Time-reversal

The *time-reversal* PSE (fig. 2.3c) is even simpler: it consists only of one hard pulse with flip angle β.[13] The catch is that the experiment must be repeated with different values of β, and the results added up with specific weightings.[5] This leads to cancellation of *some*, but not all, of the unwanted coherences: for example, on its own, it does not suppress COSY-type coherence transfer such as $I_{1-}I_{2\alpha} \rightarrow I_{1\alpha}I_{2+}$. This proved to be inconsequential in the original application of F_1 decoupling in a 2D NOESY;[13] however, it is not acceptable in a 1D context as it leads to substantial artefacts. This will be discussed in more detail in § 2.5, so a fuller analysis of the time-reversal PSE is deferred until then.

PSYCHE

Finally, we come to the PSYCHE method, which is generally considered the current state of the art for pure shift NMR.[34] The corresponding PSE (fig. 2.3d) consists of two swept-frequency pulses applied during a weak gradient: for example, a pair of chirps with opposite sweep directions can be used. Using two *saltire pulses*, pulses which simultaneously sweep in both directions, leads to an increased signal-to-artefact ratio.[35] The operation of this PSE is not easy to fully explain.[36] However, we can adopt the (not fully accurate, but still useful) instant-flip approximation[48,49]—that the swept-frequency pulse acts as an instantaneous 180° rotation on each frequency it passes through. Using this, the PSYCHE element (or strictly, the PSYCHE JRE, including a hard 180° pulse) may be viewed as a spatially parallelised version of the anti z-COSY experiment,[14,15] which we now describe.

2.2.3   PSYCHE in detail

The anti z-COSY experiment utilises a β–zero-quantum filter (ZQF)–β mixing period (fig. 2.4a), where β is a small angle, typically 10° to 20°. The role of the ZQF[50] is to remove terms such as $I_{1-}I_{2+}$ between the two β pulses, retaining only population terms such as $I_{1\alpha}I_{2\alpha}$. The CTPs

---

[*]In fact, the sensitivity is increased by the collapse of multiplet structure.

Figure 2.4: A closer look at the mechanism of the PSYCHE PSE. **(a)** The β–ZQF–β mixing period used in the original anti z-COSY experiment. This has a similar action to a JRE, but does not suppress COSY-type coherence transfers from spin i to spin j. **(b)** An illustration of how COSY-type artefacts are suppressed by the PSYCHE pulse element. The desired CTP which remains on spin 1 is rephased by the gradients, but the COSY CTP is dephased. **(c)** An illustration of how zero-quantum terms are suppressed by the PSYCHE element through spatial averaging: in each slice of the sample (highlighted in blue and orange), the zero-quantum terms are allowed to evolve for a different duration.

which this mixing period selects for ultimately give rise to peaks which lie perpendicular to the main diagonal of the spectrum. In an elegant paper, Pell et al.[15] showed that by isolating the diagonal peaks of a 2D anti z-COSY experiment and taking the 45° projection of these, a pure shift spectrum could be obtained. Here, we will go one step further and consider the *direct* use of this element as a JRE: this will reveal some problems which are neatly taken care of by the PSYCHE experiment.

We first need to introduce how the basis operators $\{I_+, I_-, I_\alpha, I_\beta\}$ evolve under a hard pulse (applied along the x-axis) with flip angle β:

$$I_\pm \xrightarrow{\beta I_x} c^2 I_\pm + s^2 I_\mp \pm \frac{iS}{2}(I_\alpha - I_\beta) \qquad (2.27)$$

$$I_\alpha \xrightarrow{\beta I_x} c^2 I_\alpha + s^2 I_\beta + \frac{iS}{2}(I_+ - I_-) \qquad (2.28)$$

{eq:ialpha_beta_evolut

$$I_\beta \xrightarrow{\beta I_x} c^2 I_\beta + s^2 I_\alpha - \frac{iS}{2}(I_+ - I_-) \qquad (2.29)$$

{eq:ibeta_beta_evoluti

where $S = \sin\beta$, $s = \sin(\beta/2)$, and $c = \cos(\beta/2)$. Using these formulae, we can show that for a two-spin system (see Pell et al.[15] for the equivalent analysis on a three-spin system), the β–ZQF–β element converts the term $I_{1+}I_{2\alpha}$ to

$$I_{1+}I_{2\alpha} \longrightarrow \underbrace{\frac{1}{2}S^2 c^4 I_{1+}I_{2\beta}}_{\text{term 1}} + \underbrace{S^2 c^2 s^2 I_{1+}I_{2\alpha}}_{\text{term 2}} - \underbrace{\frac{1}{4}S^2 c^4 I_{1\alpha}I_{2+} + \frac{1}{4}S^2 c^4 I_{1\beta}I_{2+}}_{\text{terms 3 and 4}} + \cdots, \qquad (2.30)$$

{eq:anti_z_cosy_transi

where other terms with different coherence orders have been neglected (on the basis that they can be easily suppressed with bracketing CTP gradients), and terms with higher orders in s have

been discarded since $s = \sin(\beta/2) \ll 1$ for small β.

The first term $I_{1+}I_{2\beta}$, corresponding to the flipping of passive spins only, is the only term we want to see from a JRE. The second term, $I_{1+}I_{2\alpha}$, corresponds to the case where neither active nor passive spins have been flipped. In the original anti z-COSY work, these give rise to 'off-diagonal' peaks which are part of a multiplet on the diagonal, but when projected at 45° generate artefacts around the pure shift peak. In the context of pure shift NMR, these are called 'recoupling artefacts', as they arise from imperfect J-refocusing. Note that the ratio of recoupling artefacts to desired signal is proportional to $S^2c^2s^2/S^2c^4 = \tan^2(\beta/2)$: using a smaller value for β therefore leads to better signal-to-artefact ratios, but also lower overall sensitivity. The PSYCHE element is similar to the β–ZQF–β element in this regard: it does not suppress the recoupling artefacts, but instead relies on the user choosing a suitable value for β such that the artefact-to-signal ratio is tolerably small. If the sensitivity proves to be insufficient, the flip angle β may be increased instead: this leads to a larger artefact-to-signal ratio, but if the sample is not concentrated anyway, it may well be that the artefacts do not rise above the noise level.

The third and fourth terms, $I_{1\lambda}I_{2+}$ ($\lambda \in \{\alpha, \beta\}$), represent 'COSY-type' coherence transfer to a coupled spin. In the original anti z-COSY, these led to crosspeak multiplets at (Ω_1, Ω_2), which could be removed by hand before taking the projection. However, in a pure shift sequence, the peaks arising from these terms cannot simply be removed in the same way. It is precisely this issue which precludes the β–ZQF–β element from being directly used as a JRE, and motivates the development of the PSYCHE PSE, which *does* suppress these coherence transfers.

To understand how this occurs, we invoke the instantaneous spin-flip assumption. Each coherence I_{i+} is converted (or 'flipped') to a population term $I_{1\lambda}$ at a specific point $\alpha\tau_{\text{p}}$ after the start of the first chirp, and can be reconverted to a coherence on the same spin I_{i-} at a time $\alpha\tau_{\text{p}}$ before the end of the second chirp (the blue CTP in fig. 2.4b).[*] Here, τ_{p} is the duration of the chirp, and $0 < \alpha < 1$. In this case, the coherence is perfectly rephased by the weak gradient applied during the chirp pulses, since the *time* it experiences these gradients for is the same on both sides of the chirps. Now, if the I_{i+} term is instead converted to a coherence on a different spin I_{j-}, it experiences the gradient for a total duration of $\alpha\tau_{\text{p}}$ after the start of the first chirp, and also $\alpha'\tau_{\text{p}}$ before the end of the second chirp (the orange CTP in fig. 2.4b). In general, $\alpha \neq \alpha'$ as spins i and j have different offsets; therefore, this CTP is dephased by the gradients, resulting in suppression of the COSY-type artefacts in the spectrum.

It remains to also consider how the PSYCHE element selects for the population terms between the two spin flips. Any terms with nonzero coherence order are of course simply dephased by the weak gradient. However, zero-quantum terms (in homonuclear systems) are not dephased

---

[*]Note the change in the sign of the coherence, which differs from the analysis of the anti z-COSY experiment. This arises because we are only considering the PSYCHE PSE on its own, *not* the JRE.

by gradients, and to eliminate them in a single-scan manner, they must be spatially averaged, for example by a ZQF. It turns out that the PSYCHE element also results in a similar spatial averaging. Following on from the previous paragraph, the time *between* the spin flips (for the desired pathways, i.e. not COSY-type coherence transfer) is given by $2(1-\alpha)\tau_\mathrm{p}$. At the same time, the weak gradient induces a range of offsets across the sample, much like in the Zangger–Sterk experiment. Thus, the offset, and thus the value of α, for a given spin depends on which slice it is in; for example, fig. 2.4c uses values of α_1 and α_2 for two different slices (blue and orange). If zero-quantum terms are present between the spin flips, they evolve during this time and accrue a spatially-dependent phase: summation of these during FID acquisition leads to a cancellation of these terms. Only population terms such as $I_{1\alpha}I_{2\alpha}$ survive during this, as they do not precess during this time.

The sensitivity of PSYCHE is significantly better than for other methods: depending on the flip angle β chosen, c is typically on the order of 0.05–0.15 (see also fig. 2.5 for explicit simulations). Furthermore, it is generally more robust with respect to strong coupling compared to other pure shift methods (artefacts from strong coupling often arise due to unexpected coherence transfer,[4] which is suppressed in a similar way to the COSY-type artefacts). These two factors alone have meant that PSYCHE has enjoyed substantial adoption since its introduction: a large number of 2D experiments utilising PSYCHE decoupling in either F_1 or F_2 have been developed,[22,51–56] notably the PSYCHE-iDOSY diffusion experiment,[57] where the increased resolution provided by pure shift spectroscopy translates into increased resolution in the *diffusion* dimension as well. Like the ZS element before it, the PSYCHE element has also been used for the acquisition of absorption-mode 2DJ spectra.[11]

Despite this success, PSYCHE suffers from one significant drawback: it cannot be used in a real-time fashion. The PSYCHE PSE is often said to select active and passive spins in a 'statistical' manner: this is because of the c^2 and s^2 terms arising from the low-flip angle pulses. What this really means is that we do not care *exactly* which spins are active and which are passive, but that a certain proportion of the spins are active and passive. Repeated application of the PSE therefore does not select for the same active spins each time, which precludes its application to real-time acquisition.

Although the PSYCHE PSE may appear deceptively simple at first glance, the closer analysis given here (and elsewhere[35]) clearly shows that its inner workings are anything but. Along with other ingenious experiments such as the ZQF,[4] ultrafast NMR,[58–60] and more recently GEMSTONE,[61] PSYCHE is a prime example of how *spatiotemporal averaging* and pulsed field gradients can be used to great effect in modern NMR spectroscopy.[62]

At the same time, PSYCHE itself is not *perfect*: it does not fully suppress recoupling artefacts, and can only be used in the interferogram mode. To improve on PSYCHE would therefore entail

one of the following:

1. increasing the sensitivity (while maintaining purity);

2. increasing the purity (while maintaining sensitivity); or

3. developing a pure shift element which is compatible with real-time acquisition while giving comparable sensitivity and purity to PSYCHE.

The sections which follow describe my efforts towards objectives (1) and (2).

2.3 PSYCHE with a variable number of saltires

sec:pureshift__nsaltire

Figure 2.5: Simulated signal and artefact intensity for various PSYCHE-style PSEs as a function of the flip angle used. Calculations were performed on a two-spin system with a coupling of 7 Hz, and an offset difference of 1.5 kHz. The total PSE duration was 30 ms (so, for example, in the four-saltire PSYCHE, each saltire was 7.5 ms). Solid lines indicate the coefficients for the desired $I_{1+}I_{2\alpha} \to I_{1-}I_{2\alpha}$ pathway which contributes to the pure shift signal; dashed lines the coefficients for the undesired $I_{1+}I_{2\alpha} \to I_{1-}I_{2\beta}$ pathway, which gives rise to recoupling artefacts.

The first attempted method was to change the number of saltire pulses used in the PSYCHE PSE. As described in § 2.2.3, PSYCHE relies on spatiotemporal averaging to suppress unwanted artefacts: this crucially relies on the fact that the pulse(s) used in the PSE are symmetric. This can be accomplished with two opposing chirps, or two saltires, both of which are symmetric.

However, a *single* saltire is also symmetric in itself: it is not hard to show that a single saltire can provide the requisite averaging. Likewise, the use of four saltires would also be valid.

Theoretical simulations show that the overall profile of signal and artefact versus flip angle varies with the number of saltires (fig. 2.5). Generally, using a larger number of saltires but with a smaller flip angle accomplishes a similar sensitivity level. This may be qualitatively rationalised as more saltires providing more possible CTPs which generate the desired signal (the same idea is generally invoked when discussing the difference between unidirectional chirps and saltires[35]). However, regardless of the number of saltires, the fundamental strategy of adjusting the flip angle to control the signal-to-artefact ratio remains valid, which naturally raises the question of whether specific waveforms and flip angles can be chosen in order to obtain the best decoupling quality.

Quadruple-saltire PSYCHE

The quadruple-saltire PSYCHE was first evaluated experimentally. In the first instance, I set the total duration of the PSE to 30 ms, meaning that each saltire was 7.5 ms long. In this experiment, the sensitivity was defined as the maximum height of the main peak in fig. 2.6a, and the artefact as the mean of the maximum heights of the two artefacts surrounding it. The plot in fig. 2.6b shows how these quantities vary as a function of the flip angle. Interestingly, for the artefacts, the profile observed is similar to that in the simulations: the double-saltire version performs better at low and very high flip angles, but in the middle there is a region where the quadruple-saltire version has lower artefact intensity. The signal intensities for both the double- and quadruple-saltire versions, however, seem to plateau off rather more quickly than the simulations suggest.

To highlight one particular data point, fig. 2.6b suggests that the quadruple-saltire experiment with $\beta \approx 55°$ has a similar artefact level to the double-saltire experiment with $\beta \approx 20°$, but with substantially greater signal intensity. Insets from these two spectra are respectively shown in figs. 2.6c and 2.6d. This conclusion does indeed seem to be true for the specific peak used for this analysis, which is at the right edge of the spectral insets shown here. Overall, the quadruple-saltire 55° experiment does have better sensitivity than the double-saltire 20° experiment. However, the artefacts are not always suppressed as nicely as in the chosen reference peak: for example, the peak at 4.05 ppm is significantly less clean in the quadruple-saltire experiment. Any apparent advantage over the double-saltire experiment is therefore not very clear—at least from this data alone.[*]

---

[*]In fact, I also performed some preliminary experiments where the four-saltire PSE was lengthened to 60 ms. The artefact behaviour in these spectra were better than in their 30 ms counterparts, which is to be expected since a longer PSE leads to better spatiotemporal averaging. However, I unfortunately did not compare these against a 60 ms double-saltire experiment, so these results are not included in this thesis. (It would be rather unfair to compare them against the 30 ms double-saltire.)

Figure 2.6: **(a)** The peak in the pure shift spectrum of andrographolide used for calculation of signal and artefact intensity. The recoupling artefacts flanking the main peak are clearly visible. **(b)** Peak heights of the desired signal (the central peak, solid lines) and artefacts (the mean of the two flanking peaks, dashed lines), as a function of flip angle. **(c)** Quadruple-saltire PSYCHE with $\beta = 55°$. **(d)** The reference spectrum, a double-saltire PSYCHE with $\beta = 20°$. The peak at 3.85 ppm used for the sensitivity and purity analysis is labelled with an arrow. *Data code:* `7A-201016`.

Single-saltire PSYCHE

Moving on to the single-saltire case, in addition to searching for a better signal and artefact profile as before, another possible motivation would be that the duration of the PSE can be decreased. This would minimise losses due to relaxation and diffusion during the PSE, which were not taken into account in fig. 2.5 (and the simulations there did not vary τ_p anyway). A single-saltire PSYCHE experiment was thus recorded with various combinations of flip angle ($\beta/° \in \{15, 20, 25, 28, 30\}$) and pulse duration ($\tau_p/\text{ms} \in \{15, 25, 30, 35, 45, 55\}$). In a similar way to the quadruple-saltire study, the sensitivity was defined as the maximum height of the main

peak in fig. 2.7a,[*] and the artefact as the mean of the heights of the two artefacts surrounding it. (However, note that the sample used was different.) The purity, or signal-to-artefact ratio, is simply the former divided by the latter.

Figure 2.7: **(a)** The peak in the (reference, double-saltire) pure shift spectrum of cyclosporin used for calculation of signal intensity and signal-to-artefact ratio. **(b)** Plot showing the signal intensity and signal-to-artefact ratio obtained in various single-saltire PSYCHE experiments, normalised against the double saltire experiment with $\beta = 20°$ and $\tau_p = 30\,\text{ms}$. Each line represents a series of single-saltire experiments acquired with the same value of β; τ_p generally decreases going left to right (i.e. a longer pulse means less signal). *Data code:* `5C-190617`.

The results thus obtained are shown in fig. 2.7b. In this plot, both the sensitivities as well as the signal-to-artefact ratios are normalised with respect to the reference double-saltire experiment (black dot at $(1, 1)$, acquired using $\beta = 20°$ and a total $\tau_p = 30\,\text{ms}$, i.e. 15 ms per saltire). An ideal PSE would fall in the top-right corner of this plot. Clearly, as the flip angle increases, the sensitivity increases but at the cost of the purity: this is hardly unsurprising given that the double-saltire experiment has the same property. The effect of the pulse duration is less clear-cut: in general, a shorter PSE yields to increased signal, and very usable results were obtained even with a simple 15 ms single-saltire PSE. However, a shorter PSE also leads to poorer spatiotemporal suppression of artefacts depends and thus poorer purity.

While there is no standout candidate which is *clearly* better than the double saltire (i.e. greater sensitivity as well as purity), the single-saltire pulse with $\beta = 28°$ and $\tau_p = 30\,\text{ms}$ comes close in performance to the double-saltire experiment. (The use of $\beta = 28°$ here is not coincidental: this flip angle for a single saltire was chosen to (approximately) match the sensitivity of the $\beta = 20°$

---

[*]As an alternative, the Bruker `sinocal` AU programme was also used to measure the sensitivity of the spectrum; it yielded extremely similar results, so is not shown here. I found the `sinocal` routine to be rather unreproducible as the exact value calculated depends on random noise.

double-saltire experiment.) Therefore, this does at least prove that a single saltire can be used as a PSE. However, both the single- and quadruple-saltire cases suffer from the classic dilemma of pure shift NMR: just as in the original PSYCHE, and in the Zangger–Sterk method before it, there is a compromise between sensitivity and purity, and one can only be increased at the cost of the other. Arguably, then, there is not much value in changing the number of saltire pulses as simply varying the *flip angle* of the basic double-saltire already gives the experimentalist a way to balance these competing objectives.

2.4 Direct optimisation of PSYCHE waveform

The changes to the PSYCHE waveform discussed in the previous section—changing the number of saltire pulses to either 1 or 4—are fairly minor, in that they do not fundamentally alter the form of the PSE. Furthermore, there is an obvious issue in that the quality of the spectrum is not measured in a particularly rigorous manner. Ideally, we would like to have a mathematical way of measuring how well the pure shift sequence has worked. Such a metric would also enable a more automated optimisation process, where a programme is allowed to find the best PSE without any interference from human subjectivity.

In this section, I discuss more radical changes which depart from the tried-and-tested saltire pulse. I also show how two different *cost functions*—functions which determine how 'bad' a spectrum is—can be used to objectively evaluate PSEs. Although the work in this section did not quite yield any groundbreaking results, it provided substantial insights into the nature of pure shift optimisations, which were later used in the context of POISE (chapter 3).

2.4.1 Techniques for pure shift optimisations

Throughout this chapter (and more generally this thesis), various algorithms are used for *optimisation*: that is, to find the parameters $\mathbf{x} \in \mathbb{R}^n$ which minimise a *cost function* $f : \mathbb{R}^n \to \mathbb{R}$. These algorithms can loosely be categorised as either *derivative-based* or *derivative-free*: the former use extra information in the form of ∇f to help locate the optimum, whereas the latter do not, using only the value of $f(\mathbf{x})$. While derivative-based algorithms typically converge to an optimum more quickly, they are unsuitable for problems where the cost function f is noisy. In this section, the Nelder–Mead (NM) simplex algorithm[63] was used: it is a very popular derivative-free method, and although mathematical convergence is not guaranteed,[64] in practice such cases are rather unlikely to arise. In this section, the implementation of the NM algorithm in the Python `scipy` package was simply used as-is.

The cost function measuring the performance of a pure shift experiment can be measured in one of two ways: either *theoretically*, in that the pure shift experiment is simulated using the

density operator formalism, or *experimentally*, in that the experiment is run on a spectrometer. Unfortunately, the simulation of PSYCHE-type PSEs, where a shaped pulse is applied together with a gradient, requires a large amount of time. The pulse itself already has $m \sim 10000$ points, but on top of that, the application of gradients also requires splitting up the sample into multiple slices ($n \sim 100$ to 1000) such that the evolution of ρ can be simulated in each slice and the results summed up. To make matters worse, H_{pulse} does not commute with H_{grad}, so a propagator

$$U(i, z) = \exp\left[-i(H_{\text{grad}}(z) + H_{\text{free}} + c_x^{(i)}I_x + c_x^{(i)}I_y)(\delta t)\right] \qquad (2.31)$$

must be calculated for each pulse point, in each slice of the sample, for a total of mn matrix exponentials. As a result, the simulation of PSYCHE spectra in the Spinach package[65] typically requires minutes to hours.*

This in fact makes it faster to experimentally acquire a pure shift spectrum and calculate a cost function based on that. Running an actual pure shift experiment, though, is suboptimal: firstly, the pseudo-2D interferogram method is slow, and secondly, there is no easy way to devise a cost function for the resulting spectrum without prior knowledge of where peaks and artefacts lie. Instead, we can use a simple 1D 'J-refocused spin echo' (JRSE) sequence, which has the form 90°–τ–PSE–τ–detect (fig. 2.8b). An ideal PSE would lead to complete refocusing of both chemical shifts and J-couplings, and the signal detected after this would simply be the same as in a pulse–acquire experiment (fig. 2.8a).

Of course, there is a sensitivity penalty which reflects that of the PSE (there are also relaxation losses during the τ delays, but these are a constant, unaffected by the form of the PSE). On top of that, if the J-refocusing is not perfect, then the multiplets in the spin echo sequence acquire a degree of phase distortion: the delay τ has to be long enough to allow for this to evolve, but its exact value is otherwise largely insignificant. These distortions are just about visible in fig. 2.8b.

Two cost functions were designed and used in this section:

$$f_{\text{phase}} = \text{Var}_i\left[\arctan\left(\frac{S_{\text{re},i}}{|S_{\text{im},i}|}\right)\right] \qquad (2.32)$$

$$f_{\text{diff}} = \left\|\frac{S_{\text{re}}}{\|S_{\text{re}}\|} - \frac{T_{\text{re}}}{\|T_{\text{re}}\|}\right\|, \qquad (2.33)$$

where the JRSE and pulse–acquire 1D spectra are treated as complex-valued vectors S and T respectively (for '*spectrum*' and '*target*'). S_{re} and S_{im} are the real and imaginary parts of the

---

*With highly optimised handwritten code, exploiting the symmetry of the PSYCHE element, the fastest simulation I could do took 16 seconds on a 20-core computer, for a simple 2-spin system. This number increases exponentially for larger spin systems. It is possible that GPU acceleration could result in substantial speedups, but I have not looked into this sufficiently. Anyway, acquisition of the JRSE experiment (to be described) takes only around 5 seconds.

./figures/pureshift/jrse.png

Figure 2.8: **(a)** Pulse–acquire experiment and the resulting spectrum. **(b)** J-refocused spin echo experiment and the resulting spectrum. The PSE used was the PSYCHE double saltire, with a flip angle of 25°; the delay τ was 11 ms. The OH peak at 4.1 ppm is lost, most likely due to chemical exchange. *Data code:* 6A-200816.

spectrum S, and $S_{\mathrm{re},i}$ is the i-th point of the real part of the spectrum. The operator Var_i represents the variance over all points in the spectrum i, and $\|\mathbf{x}\|$ denotes the 2-norm of the vector $\mathbf{x}$, i.e. $\sqrt{\sum_i x_i^2}$. Python implementations of these are given in listing 2.1.[*]

```python
import numpy as np
# assume S and T are complex numpy arrays which have been read in
Sr = np.real(S); Si = np.imag(S); Tr = np.real(T)
f_phase = np.var(np.arctan(Sr / np.abs(Si)))
f_diff = np.linalg.norm((Sr / np.linalg.norm(Sr))
                        - (Tr / np.linalg.norm(Tr)))
```

Listing 2.1: Pure shift cost functions.

These two cost functions were chosen as they exhibited desirable characteristics on synthetic data (fig. 2.9). In these simulations, the 'target' spectrum was chosen to simply be an in-phase absorption-mode doublet with an SNR of 500. Synthetic data with increasing amounts of J-modulation (i.e. spectra ranging from in-phase absorption, to antiphase dispersion) were generated, and extra Gaussian noise added to mimic different SNRs. It can be seen that, for data which has little J-modulation (left edges of the plots), both f_{phase} (fig. 2.9a) and f_{diff} (fig. 2.9b) penalise lower SNRs. Furthermore, both of the cost functions penalise J-modulation, since they increase going from left to right. This penalty is stricter for high-SNR spectra, which is also

---

[*]The use of np.arctan (the arctangent), and *not* np.arctan2 (the argument of a complex number), is intentional. The behaviour shown in fig. 2.9 isn't reproduced with arctan2. Of course, this means the name 'phase' is a misnomer; it's not really the phase of anything meaningful.
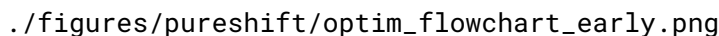
Figure 2.9: Behaviour of the two cost functions, f_{phase} and f_{diff}, on synthetic spectra with various SNRs. Zero phase distortion refers to an in-phase absorption-mode doublet, whereas complete phase distortion refers to an antiphase dispersion-mode doublet. **(a)** The f_{phase} cost function. **(b)** The f_{diff} cost function, measured against a spectrum with no phase distortion and an SNR of 500.

desirable, since it is only in high-SNR spectra that the J-modulation becomes noticeable.

The cost function f_{diff} is easier to comprehend: it simply scales both the target and JRSE spectra down by their respective intensities, and compares each point to determine whether the peak shapes obtained are similar. Although this seems like it should be agnostic towards signal intensity, this is only true for noiseless spectra. If a (genuine) JRSE spectrum has low SNR, $\|S_{\text{re}}\|$ will be small, and the noise will be scaled down less than for the target spectrum; this difference in the *noise* (rather than the signal) then contributes towards the cost function. On the other hand, a proper rationalisation of why the cost function f_{phase} works is unfortunately not within my capabilities! It was mostly developed by trial-and-error (based on the notion that phase distortions would have something to do with S_{re} and S_{im}), and I do not have a good explanation of why it works.

The general optimisation procedure is conceptually simple and largely consists of the loop shown in fig. 2.10: this is essentially a specialised version of the POISE flowchart (fig. 3.1). The optimisation algorithm is responsible for determining convergence, as well as choosing the new parameters based on previously obtained information; the initial parameters must be supplied by the user.

In practice, it is a technical challenge to implement this loop on a spectrometer as the cost function

Figure 2.10: Flowchart illustrating the steps for optimisation of a pure shift spectrum.

calculation is performed either in Matlab or Python 3, both of which are not compatible with Bruker's TopSpin software. TopSpin instead provides Jython (Python 2.7) and C programming interfaces;[*] the former is not compatible with Python 3 packages like numpy or scipy, and the latter is too low-level to be worth implementing numerical algorithms in.[†] Thus, we require a means of *communication* between the spectrometer and the optimisation control programme: this includes a signal from the controlling programme to trigger acquisition on the spectrometer, as well as a signal from the spectrometer that acquisition is done so that the cost function can be calculated. As it turns out, the code used for the optimisations in this section was a very rudimentary and fragile form of that eventually used in POISE (for example, the aforementioned signals were transmitted via the creation and deletion of files). I therefore defer the discussion of this issue to § 3.2.5, where the more robust POISE interface is explained in detail.

2.4.2 Flip angle optimisation

Having described the rest of the optimisation setup, it remains to choose exactly which parameters are subjected to optimisation. The simplest option is to only optimise one parameter, namely the flip angle of the (double-)saltire pulse. The flip angle dependence of PSYCHE spectra is well-understood, which crucially allows us to evaluate the cost functions outlined above and determine whether they are functioning correctly.

I first sought to measure how the cost functions described above varied with the flip angle. To this end, JRSE spectra using a *single* saltire as the PSE and various flip angles (from 10° to 50°) were acquired (fig. 2.11). Since both cost functions penalise both low sensitivity and low purity, we might expect that there is be an intermediate value where neither sensitivity nor purity were

---

[*]TopSpin 4.1.4 introduced a Python 3 interface which would have made much of this work simpler. Unfortunately, this was not available at the time of this work.

[†]Of course, heavily optimised code in low-level languages such as C and Fortran—or perhaps even Matlab—would run faster. However, speeding up the code has virtually no impact on the optimisation, since its rate is limited by spectrum acquisition. In this situation, it makes far more sense to save *developer time*.

Figure 2.11: Behaviour of the two cost functions, f_{phase} and f_{diff}, on experimental J-refocused spin echo spectra. *Data code:* `5C-190809`.

penalised too much: this would the 'optimum' flip angle. In the event, it was found that only f_{diff} yielded a useful—albeit shallow—minimum at around 25° (recall that the PSE here is a single saltire, so this corresponds roughly to a 15°–20° double saltire). The f_{phase} cost function, on the other hand, was strictly decreasing within the range of flip angles tested: it is possible that there is an optimum at an even larger flip angle, but this would have been a scientifically unsound conclusion given that the sample was decently concentrated (50 mM).

This naturally raises the question of why f_{diff} yields an optimum which falls within what we would consider a 'sensible' region. It is tempting to believe that the form of f_{diff} (eq. (2.33)), which is at first glance quite intuitive, naturally leads to a better result. I argue here, however, that this is mostly down to *coincidence*. This is difficult to explain quantitatively, but in a broader sense, we may imagine that the cost function separately penalises low sensitivity and low purity, i.e. it can be decomposed into something of the form

$$f = g(s) + \lambda h(p), \tag{2.34}$$

where s and p are respectively the sensitivity and purity, and g and h are some unknown functions which *decrease* with increasing s and p (since we want to minimise the cost function). This is clearly a simplification, because the plots in fig. 2.9 show that the effects of sensitivity and purity on the cost functions are not additive; however, it is sufficient to make the point here. The parameter λ represents the relative weighting of purity to sensitivity: if λ is large than the purity is more strongly emphasised, and vice versa if λ is small.

When we say that an optimum is 'sensible' or 'sound', this is with respect to the sensitivity/purity balance in the parent pseudo-2D homodecoupled spectrum. In other words, what we *really* seek

is a cost function which measures the sensitivity and purity of that spectrum:

$$f' = g'(s') + \lambda' h'(p'), \tag{2.35}$$

{eq:cost_function_gene

where everything is marked with a prime symbol to indicate that it is with respect to the decoupled spectrum, and the parameter λ' is chosen to fit our judgement of the required balance, or in other words, yield an optimum of around 20°. Now, we may reasonably assume that s and s' are proportional, but p and p' are hardly the same thing: one is manifested in terms of artefact intensity and the other in terms of phase distortions. Furthermore, the λ provided to us by the cost function f may not necessarily be the same as our ideal choice of λ'; let alone the forms of the functions g and h. The fact that eq. (2.34) *happens* to provide the same flip angle optimum as the idealised eq. (2.35) cannot truly be attributed to design!

Of course, just because a cost function works mostly by serendipity does not mean that it cannot be used. So, I ran several *actual* optimisations of the flip angle using the cost function f_{diff}, which reliably converged to optima between 20° and 25° regardless of the initial point chosen. Typically, around 10 spectrum acquisitions were required, corresponding to a time of around 2–4 minutes. This is not surprising in light of our knowledge of f_{diff}; however, it provides us with a proof-of-principle that automated optimisation of NMR parameters is possible. Further optimisations of the PSYCHE flip angle are also discussed in § 3.4.8.

2.4.3   Waveform parameterisation and optimisation

ec:pureshift__chirpopt

Given that a working optimisation setup, including cost functions, had been developed, it was a logical step to then test it out on a more challenging problem: namely, how the waveform used in the PSYCHE PSE could be modified. This goes beyond simply modifying the number of saltires, as was done in § 2.3. There is no real reason why the pulse *must* be an integer number of saltires: in principle it can have *any* shape, although being symmetric about the centre of the pulse would likely still be beneficial in terms of preserving the mechanism of spatiotemporal averaging.

Sum-of-chirp parameterisation

A naive attempt at optimising the pulse would simply involve modifying every pulse point in the double-saltire waveform used in the PSYCHE element. As described in § 1.2, each pulse point consists of a pair of x- and y-amplitudes (c_x, c_y); therefore, for a pulse with m points, we would have a parameter vector $\mathbf{x} \in \mathbb{R}^{2m}$. Unfortunately, for PSYCHE, m is on the order of 10000, and

an optimisation with 20000 points is totally unfeasible.[*]

As a result of this, we must consider other ways of parameterising the waveform which use fewer degrees of freedom. Several approaches to this issue have surfaced in the literature, such as the use of Fourier series,[37,70–73] Gaussian cascades,[74] or spline interpolation between a subset of pulse points.[75] In this instance, we can use the knowledge that the PSYCHE PSE is composed of saltire pulses to our advantage. Each saltire pulse is a linear combination of two chirps, defined by:

$$\phi(t) = \phi_0 + 2\pi f_0 t + \pi \tau_{\mathrm{p}} (\Delta F) \left(\frac{t}{\tau_{\mathrm{p}}} - \frac{1}{2} \right)^2 \tag{2.36}$$ {eq:chirp_pulse_phase}

$$c_x(t) = A \cos[\phi(t)] \tag{2.37}$$ {eq:chirp_pulse_cx}

$$c_y(t) = A \sin[\phi(t)] \tag{2.38}$$ {eq:chirp_pulse_cy}

for $t \in [0, \tau_{\mathrm{p}}]$. Here, τ_{p} is the duration of the chirp, A is the amplitude of the chirp (which is time-independent), ϕ_0 the phase of the chirp, ΔF the bandwidth, and f_0 its frequency offset (i.e. where the centre of the bandwidth lies). The latter two parameters are assumed to be given in units of ordinary frequencies (Hz), not angular frequencies. (Note that eqs. (2.37) and (2.38), defining the x- and y-coefficients of the pulse, are just a restatement of eq. (1.30).)

Figure 2.12: Plots of the quantities in eqs. (2.36) to (2.38) for a typical chirp pulse ($\tau_{\mathrm{p}} = 30\,\mathrm{ms}$, $\Delta F = 10\,\mathrm{kHz}$). **(a)** $\phi(t)$ wrapped to the range $[0, 2\pi)$. **(b)** The quarter-sine smoothing profile which is later applied to the entire waveform (eq. (2.39)); here $s_{\mathrm{sm}} = 0.2$. **(c)** $c_x(t)/A$ prior to smoothing. **(d)** $c_y(t)/A$ prior to smoothing. The amplitude A is simply a constant, which is related to the flip angle of the chirp.[35]

---

[*]Although problems of this size have been tackled using optimal control theory,[66–69] it is not really feasible to use it in cases where the pulse is applied *together* with a gradient, as is the case in PSYCHE. On top of that, the coupling networks and spin systems of interest are rather more complicated than in typical applications of optimal control.

Given these expressions, we see that there are five parameters of the chirp which can be modified: A, τ_p, ϕ_0, ΔF, and f_0. The two chirps which form one saltire pulse simultaneously sweep in opposite directions, which mean that ΔF for one chirp is the negative of the other; however, their parameters are otherwise equal. We may, however, also envision a case where the pulse is constructed from two chirps which are applied at a different point in time. This adds one more parameter to each chirp, namely t_0, the starting time of the pulse) Each chirp therefore sweeps from the frequency $f_0 - (\Delta F)/2$ at a time t_0, to the frequency $f_0 + (\Delta F)/2$ at a time $t_0 + \tau_p$. In total, this gives us 12 parameters to optimise.[36,76]

After constructing the sum of two chirps, 'empty' regions of no RF application ($c_x = c_y = 0$) at the beginning and the end were trimmed off. Since a sum of two chirps is not necessarily symmetric (with respect to reflection in time), the waveform was then reflected about its end, thus doubling the length of the pulse. The entire waveform was then multiplied by a *smoothing function* $f_{sm}(t)$ (fig. 2.12b), which prevents large jumps in RF amplitude at the beginning and end of the pulse. f_{sm} depends on a smoothing parameter s_{sm}, which is typically 0.1–0.2:

$$
f_{sm}(t) = \begin{cases} \sin\left(\dfrac{\pi t'}{2 s_{sm}}\right) & 0 \leq t' < s_{sm}; \\ 1 & s_{sm} \leq t' < 1 - s_{sm}; \\ \sin\left[\dfrac{\pi(1 - t')}{2 s_{sm}}\right] & s_{sm} \leq t' \leq 1, \end{cases} \tag{2.39}
$$
{eq:sming_function}

where $t' = t/\tau_p$ (and here τ_p refers to the duration of the *entire* waveform, after reflection.).

Optimisations

The initial point chosen was:

- Chirp 1: $\tau_p = 15\,\text{ms}$; $\Delta F = -5\,\text{kHz}$; $\phi_0 = 0$; $A = 36\,\text{Hz}$; $t_0 = 0$; $f_0 = 5\,\text{kHz}$;

- Chirp 2: $\tau_p = 15\,\text{ms}$; $\Delta F = 5\,\text{kHz}$; $\phi_0 = 0$; $A = 36\,\text{Hz}$; $t_0 = 0$; $f_0 = -5\,\text{kHz}$.

After the sum of these two pulses is reflected about its end, we obtain a single saltire with bandwidth 10 kHz, duration 30 ms, and an amplitude of 72 Hz, corresponding to a flip angle of approximately 32°.

Using this setup, several optimisations of the 12 parameters above were conducted using the f_{diff} cost function, which had performed well enough in the flip angle optimisations. However, it was quickly noticed that this led to spurious optima being located, such as the one in fig. 2.13c. Although the initial point (a saltire) yielded a much larger SNR (fig. 2.13b), the value of f_{diff} was still larger (i.e. worse) than for this false optimum. The reason for this is almost certainly because the saltire pulse distorts the relative intensity of the strong singlets in the spectrum, notably the

Figure 2.13: **(a)** Target spectrum (pulse–acquire). **(b)** JRSE spectrum obtained using the initial guess (a saltire). **(c)** JRSE spectrum obtained with a spurious optimum point. The grey dotted box shows the restricted region over which f_{diff} was subsequently applied to, yielding a formally different cost function f'_{diff}; this yielded more sensible results where the cost function for the saltire pulse was smaller. *Data code:* `6C-190823`.

C_6D_5H peak at 7.15 ppm, and the *N*-methyl groups between 2.5 and 3.8 ppm), whereas the false optimum does not (most likely by coincidence).

Of course, singlets are completely unimportant when devising a pure shift experiment. Unfortunately, singlets are also typically more intense than the rest of the spectrum, and thus contribute disproportionately to the cost function. A simple and effective way to circumvent this is to restrict the region of the spectrum being evaluated. In this case, I chose to use the cyclosporin H^{α} region between 4.72 and 5.94 ppm (grey dotted box in fig. 2.13). This yields a formally different cost function, which I label as f'_{diff}. With this, much more logical behaviour was observed: in particular, the saltire pulse performed better than the spurious optimum previously found.

While this new cost function could be successfully used to run optimisations, most of these unfortunately failed to find anything performing better than the original saltire pulse. On the rare occasion where something 'better' was found (as judged by the new cost function f'_{diff}), these 'optimised' pulses were fairly close to a saltire, and the corresponding decreases in the cost function extremely small—suggesting that the 'better' result may simply just have been due to noise in the cost function. Nevertheless, these new 'optima' *did* function as perfectly serviceable PSEs: for example, fig. 2.14 compares a triple spin echo (TSE) PSYCHE spectrum obtained with an 'optimised' pulse to one obtained with the single saltire pulse. There is virtually no difference. This is a meaningful result, as it demonstrates that f'_{diff} is actually an accurate metric to determine

the quality of a PSE (it is noisy, but this is to be expected of an experimentally measured cost function). Unfortunately, although the pulse shape is shown in fig. 2.14b, the exact parameters which led to this pulse shape have been lost to time.

Figure 2.14: **(a)** x- and y-coefficients of the initial saltire pulse (as a fraction of the maximum amplitude A). **(b)** x- and y-coefficients of the 'optimised' pulse (as a fraction of the maximum amplitude A). **(c)** TSE-PSYCHE spectrum obtained with the initial guess (a saltire pulse). **(d)** TSE-PSYCHE spectrum obtained with the 'optimised' pulse, with virtually equivalent performance. *Data code:* `6C-190831`.

One issue is that the optimisation algorithms used here can only perform a *local* optimisation, i.e. it may not necessarily locate a global optimum. We cannot rule out the possibility that *some* pulse within this parameter space may in fact outperform a saltire pulse. However, finding this optimum—which may lie very far away from the initial guess of a saltire pulse—is not generally something which can be accomplished in a reasonable amount of time, even though 12 parameters is far more tractable than 20000. Furthermore, although the cost functions described here do work, they are generally quite 'flat', in that they do not discriminate very sharply between 'good' and 'bad' spectra. Combined with the fact that the cost function is noisy, this makes experimental optimisation of the waveform an uphill task. Nevertheless, much of the knowledge (and code) in this section was later used in the development of POISE.

In the next two sections in this chapter, I move on from PSYCHE and instead discuss completely different methods of obtaining pure shift spectra using only hard pulses in the PSE.

2.5 Time-reversal method

This section focuses on the time-reversal element briefly introduced in § 2.2.2: the aim is to determine whether a pure shift method based on this can have better performance than PSYCHE. Before that, I will first provide a more detailed theoretical analysis of it. The time-reversal element consists of just a single hard pulse with a flip angle β, and we first analyse its potential use as a JRE (instead of a PSE), using eqs. (2.27) to (2.29).

Recall that an ideal JRE should invert passive spins only, not active spins: thus, we seek a transformation of the form $I_{1+}I_{2\alpha} \to I_{1+}I_{2\beta}$. However, the hard pulse does this:

$$I_{1+}I_{2\alpha} \to \underbrace{c^2 s^2 I_{1+}I_{2\beta}}_{\text{term 1}} + \underbrace{c^4 I_{1+}I_{2\alpha}}_{\text{term 2}} - \underbrace{\frac{S^2}{4}I_{1\alpha}I_{2+} + \frac{S^2}{4}I_{1\beta}I_{2+}}_{\text{terms 3 and 4}}, \qquad (2.40)$$

where (as before) $S = \sin\beta$, $s = \sin(\beta/2)$, and $c = \cos(\beta/2)$. As in the analysis for PSYCHE (§ 2.2.3), term 1 here represents the desired signal; term 2 recoupling artefacts; and terms 3 and 4 COSY-type artefacts arising from coherence transfer. Terms with difference coherence orders have been neglected as they can be removed using CTP gradients.* Unlike in the PSYCHE analysis, however, we have not neglected any other terms of smaller order in *s*.

Since the desired and undesired terms have different coefficients, it is possible to *fully cancel out the recoupling artefacts* by recording (in this case) two different spectra with different values of β and performing an appropriate linear combination:

$$I_{1+}I_{2\alpha} \xrightarrow{\beta=0°} I_{1+}I_{2\alpha} \qquad (2.41)$$

$$I_{1+}I_{2\alpha} \xrightarrow{\beta=90°} \frac{1}{4}I_{1+}I_{2\beta} + \frac{1}{4}I_{1+}I_{2\alpha} - \frac{1}{4}I_{1\alpha}I_{2+} + \frac{1}{4}I_{1\beta}I_{2+} \qquad (2.42)$$

If we take eq. (2.42) minus 1/4 of eq. (2.41), the recoupling artefacts (arising from the $I_{1+}I_{2\alpha}$ term) are fully removed. In general, for an *N*-spin system, there are several different 'types' of recoupling artefacts where different numbers of passive spins (between 1 and $N-1$) are not inverted. Each of these pathways will have different coefficients, as each spin that is flipped contributes s^2, whereas each spin that is not flipped contributes c^2. Suppressing all of these requires the acquisition and summation of *N* spectra with different flip angles and appropriate weights.

Before we go on further, notice even in the two-spin system that the COSY-type artefacts are *not* suppressed! In the original work,[13] this time-reversal element was used in the middle of the t_1 period in a NOESY experiment. The coherence transfer peaks were not deemed to be

---

*In the original work[13] which predated widespread use of field gradients, other terms were removed through phase cycling, which is essentially equivalent.

problematic in this context: they gave rise to artefacts which had F_1 frequencies of $(\Omega_1 + \Omega_2)/2$, but different phase properties to genuine crosspeaks, allowing them to be easily identified. Of course, these artefacts are not acceptable in an actual pure shift spectrum.

To remove these peaks, I adopted the strategy first reported by Thrippleton *et al.* for suppression of COSY-type transfer pathways in 2DJ spectra.[4] In a 2DJ experiment, the central 180° pulse should in principle not cause coherence transfers between different spins; however, in strongly coupled systems this can happen. The solution was to bracket the 180° pulse, as well as half of the t_1 period, with a pair of opposing chirps and gradients. The same idea was later used in the TSE-PSYCHE experiment[11] to (further) suppress strong coupling responses in the parent PSYCHE experiment. This works because the unwanted CTPs have coherences on different spins during each of the two chirps; consequently, the coherences are inverted at different times by the chirp pulses, and are ultimately dephased by gradients. The resulting time-reversal experiment was thus simply the same as the parent TSE-PSYCHE experiment, except that the central PSYCHE element was replaced by a β hard pulse (fig. 2.15).

./figures/pp/pureshift/timereversal.png

Figure 2.15: Time-reversal pure shift pulse sequence. The flip angle β is varied as described in eq. (2.43). Pulse phases are: $\phi_1 = (x, y, -x, -y)$; $\phi_{\mathrm{rec}} = (x, -x, x, -x)$. The delay τ is set to $1/(4 \cdot T_{\mathrm{chunk}})$, and allows for J-coupling to be refocused in the middle of the chunk. Gradient amplitudes are $(g_1, g_2, g_3, g_4) = (35\%, 49\%, 77\%, 1\%)$ (note that, in principle, g_4 should be calibrated according to the bandwidth of the chirp used).

In such a sequence, the JRE is in fact not only the β pulse itself but also the second chirp (which effectively acts as a 180° pulse). So, the β pulse here fulfils the role of a PSE, not a JRE: this means that different flip angles and weights must be chosen. As before, for a system containing N mutually coupled spins, N different experiments must be acquired using the following flip angles β_j and summed with the corresponding weights W_j ($j = 1, 2, \ldots, N$):

$$\beta_j = \frac{j\pi}{N} \tag{2.43}$$

$$W_j = \frac{N}{8} \cdot \frac{(-1)^j}{\sin^2(\beta_j/2)}. \tag{2.44}$$

For the sake of completeness, the values of β and W for a JRE are given here as well:

$$\beta_k = \frac{k\pi}{N} \tag{2.45}$$

{eq:timereversal_jre_a

$$W_k = \frac{N}{8} \cdot \frac{(-1)^{k+N}}{\cos^2(\beta_j/2)} \tag{2.46}$$

{eq:timereversal_jre_w

for $k = 0, 1, \ldots, N - 1$. The derivation of these expressions is discussed more thoroughly in a paper by Griesinger et al.[5] In the context of this specific paper, note that the weights for the PSE correspond to that used for the ECOSY experiment, and the weights for the JRE correspond to that used for the complementary ECOSY experiment.

In practice, $N = 5$ is likely to cover most realistic spin systems. Explicitly evaluating eqs. (2.43) and (2.44) yields $\beta = \{36°, 72°, 108°, 144°, 180°\}$ and $W = \{-6.545, 1.809, -0.955, 0.691, -0.625\}$. Figure 2.16 shows insets of the five subspectra acquired with the above values of β and scaled by their respective weights W. The weighted sum (i.e. the pure shift spectrum) was phased, and the resulting phase correction values were propagated back to the individual subspectra.

./figures/pureshift/timereversal_insets.png

ig:timereversal_insets

Figure 2.16: Insets of weighted time-reversal subspectra (with $j = 1$ through 5), as well as their sum (the pure shift spectrum). *Data code:* 7A-201020.

Although the experiment seems to work, in that the weighted sum *is* indeed a pure shift spectrum,

the fact that it is obtained through summation of *N* different experiments brings some immediate drawbacks. Firstly, the minimum duration of the experiment is lengthened by a factor of *N*: this is essentially the same as an *N*-step phase cycle. However, and perhaps more importantly in the context of *pure shift* NMR, the artefacts surrounding the main peaks are not perfectly cancelled through the process of summation. As a result, random distortions are observed around the desired peaks in the pure shift spectrum: this is noticeable in the 4.04 ppm peak in fig. 2.16, and is even worse for more intense signals.

In terms of sensitivity, the time-reversal spectrum is not particularly exceptional, either. Each of the five subspectra above were acquired with 2 scans; when compared against a typical TSE-PSYCHE experiment acquired with only 4 scans (i.e. 40% of the experiment duration), the TSE-PSYCHE experiment had comparable or perhaps even slightly better SNR (fig. 2.17). The likely reason for this is because in the time-reversal experiment, signal is actually being *cancelled out* through the process of summation, as is quite clearly shown in fig. 2.16. In principle, the sensitivity of the time-reversal experiment could be optimised by acquiring the more heavily weighted spectra with more scans. However, I consider this unlikely to make a substantial difference to the conclusions drawn here. The idea of re-optimising the weights to better suppress artefacts was also briefly considered. However, given that eq. (2.44) already yields *theoretically* complete suppression, it was deemed unlikely that anything substantially better could be obtained, considering that the artefacts arise from the summation process itself and are likely to appear regardless of what weights are chosen. Performing such an optimisation would also require a pure shift spectrum to have been acquired beforehand (for comparison), thus defeating the purpose of optimising the weights anyway.

Figure 2.17: Comparison of time-reversal and TSE-PSYCHE sensitivity. **(a)** Time-reversal pure shift spectrum (the same as the sum in fig. 2.16) acquired with 2 scans for each subspectrum. **(b)** TSE-PSYCHE (double saltire, flip angle 15°) acquired with 4 scans. The spectra have been scaled so that their noise levels are similar: the signal intensity is comparable, or perhaps slightly better in the TSE-PSYCHE. *Data code:* `7A-201020`.

Interestingly, fig. 2.16 suggests that the *j* = 1 spectrum *on its own* already provides as good a

result as the summed pure shift spectrum. This is not surprising, as the use of a hard pulse as the PSE yields a conceptually very similar result to PSYCHE in that the signal to artefact ratio depends on $\tan^2(\beta/2)$ (of course, the COSY-type artefacts must still be suppressed through the TSE scheme). This suggests that even without summation of multiple subspectra, the TSE time-reversal pulse sequence in fig. 2.15 is a viable pure shift experiment—albeit one which does not have any significant advantage over PSYCHE.

2.6 'Discrete PSYCHE'

The last pure shift method in this chapter is completely original, and represents perhaps the most fruitful attempt so far at optimising pure shift experiments. It relies on what is essentially a 'temporal discretisation' of the PSYCHE waveform and gradient combination: instead of applying a shaped pulse and a gradient simultaneously, hard pulses and gradients are interleaved in the PSE (fig. 2.18).
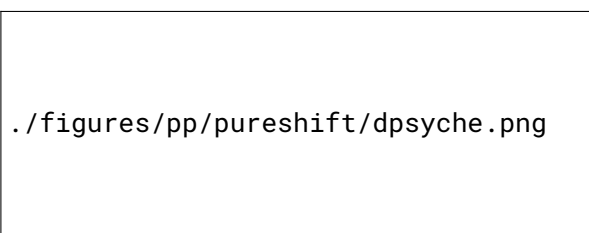
Figure 2.18: dPSYCHE pulse sequence. Gradient amplitudes are $(g_1, g_2) = (35\%, 41\%)$; the gradients in the PSE g_2 are applied with a duration of $500\,\mu s$. The hard pulses in the PSE are applied with an RF amplitude of $18\,kHz$. The delay τ is set to $1/(4 \cdot T_{\text{chunk}})$, and allows for J-coupling to be refocused in the middle of the chunk.

For this reason I have dubbed this experiment the 'discrete PSYCHE', or dPSYCHE for short. There are two major reasons why this is more amenable towards optimisation than many of the previous experiments:

1. Pulses and gradients are no longer applied simultaneously, which makes simulation of the experiment *extremely* fast compared to the original PSYCHE. This opens up the possibility of entirely theoretical optimisations, as the noise can be completely eliminated from the cost function.

2. There are much fewer 'pulse points' than in the original PSYCHE: effectively, the phase and flip angle of every hard pulse has to be optimised, leading to $2m$ parameters. Even for $m \sim 10$, this is quite tractable if the optimisation is noiseless.

One downside of this is that it is difficult, or perhaps even impossible, to explain how the PSE

works.* For a symmetric PSE where $\beta_1 = \beta_m$ (and so on) it is probably possible to reuse an explanation based on PSYCHE-style CTP selection, but this is clearly inapplicable if the flip angles and phases are scrambled.

2.6.1 Speeding up dPSYCHE simulations

To begin, I first explain how the exact simulation of dPSYCHE experiments can be greatly accelerated through efficient propagator calculations. Although Spinach[65] is the leading simulation package for NMR, and covers an extremely impressive range of experiments, this generality also prevents it from providing optimal performance for any single experiment. As it turns out, handwritten, specialised Matlab code can outperform Spinach by orders of magnitude.

The NMR simulations developed here simply use the density operator formalism in Hilbert space, as outlined in § 1.3. The Zeeman basis is used, and non-unitary transformations such as relaxation are neglected. Now, propagation under the Liouville–von Neumann equation (eq. (1.38)) requires the calculation of matrix exponentials $\exp(-iHt)$. For an $N \times N$ matrix, the matrix exponential requires $O(N^3)$ time to calculate (and for a system containing p spins, we have $N = 2^p$); it is often this which is the bottleneck in NMR simulations. Minimising the number of matrix exponentials, and/or their computational cost, is the key to achieving speedups, as will be shown in the following text.†

Generally, the accurate simulation of pulsed field gradients requires the sample to be divided up into n discrete slices, each simulated with a different H_{grad}.‡ Thus, a very naive implementation of the dPSYCHE experiment would require mn matrix exponentials, one per pulse per slice. The overall structure of the code would resemble listing 2.2. (Strictly speaking, the code is wrong because the final gradient should have strength -2G and not G, but that is a minor detail which I leave out for clarity in the code.)

It is not difficult to come up with a more sensible approach which cuts this down by a factor of m: since the pulses are not applied together with the gradients, the pulse propagators U_{pulse} can be pre-calculated outside of the loop. Furthermore, all of the gradients within the PSE are the same, so U_{grad} can be moved out of the inner loop (listing 2.3).

---

*Of course, we could simulate it and say that it works because the maths says it does; but that isn't very illuminating. Some of the optimisations done in this thesis are somewhat like a scaled-down version of machine learning, in that they produce better results at the cost of interpretability.

†Note that in my simulations, I simply used the builtin `expm` Matlab function, which implements the matrix exponential using a combination of the scaling-and-squaring method and Padé approximation.[77] This is in contrast to Spinach, which primarily uses a scaled-and-squared Taylor series (according to the `propagator.m` file, various other methods supposedly did not 'live up to their marketing'). An in-depth discussion of matrix exponential methods is outside the scope of this thesis, but can be found in a classic paper by Moler and Van Loan.[78]

‡In simple cases this can be avoided by simply removing all terms with the wrong coherence orders as we know they will be dephased (eq. (1.110)), but this is too naive an approach for pure shift techniques.

t__dpsyche_simulations

```
% loop over slices
for slce=1:n
    H_grad = I_z * G * z(slce);

    % loop over pulse points
    for pulse_point=1:m
        H_pulse = (c_x(pulse_point) * I_x) + (c_y(pulse_point) * I_y);

        % calculate propagators; m*n total matrix exponentials
        U_pulse = expm(-1j * (H_free + H_pulse) * t_pulse);
        U_grad = expm(-1j * (H_free + H_grad) * t_grad);

        rho = U_grad * U_pulse * rho * U_pulse' * U_grad';
    end
end
```

Listing 2.2: Rough structure of a naive dPSYCHE implementation. Note that I use the variable name `slce` as `slice` is an existing builtin Matlab function.

lst:dpsyche_slow

Spinach, which is designed to be general, has no idea that these optimisations are possible, so is naturally rather slower. However, even this is relatively inefficient. It can be shown that the two components of the gradient propagator, H_{free} and H_{grad}, actually commute with one another (even in the strong coupling case). Thus, we can write:

$$\exp[-\mathrm{i}(H_{\text{free}} + H_{\text{grad}})t] = \exp(-\mathrm{i}H_{\text{free}}t)\exp(-\mathrm{i}H_{\text{grad}}t) \tag{2.47}$$ {eq:split_propagator}

(in general, for matrices A and B, $\exp(A + B) = \exp(A)\exp(B)$ if and only if $[A, B] = 0$). This on its own does not reduce the number of matrix exponentials required, but notice now that H_{grad} is a sum of I_{iz} terms and is therefore *diagonal* in the Zeeman basis. The exponential of a diagonal matrix is almost trivial to calculate, as we simply need to exponentiate the diagonal *elements:*

$$\exp\begin{pmatrix} \lambda_1 & 0 & \dots & 0 \\ 0 & \lambda_2 & \dots & 0 \\ \vdots & \vdots & \ddots & \vdots \\ 0 & 0 & \dots & \lambda_n \end{pmatrix} = \begin{pmatrix} \exp(\lambda_1) & 0 & \dots & 0 \\ 0 & \exp(\lambda_2) & \dots & 0 \\ \vdots & \vdots & \ddots & \vdots \\ 0 & 0 & \dots & \exp(\lambda_n) \end{pmatrix}. \tag{2.48}$$ {eq:expm_diagonal}

Instead of using the $O(N^3)$ `expm(M)` function, this can instead be done in $O(N)$ time using `diag(exp(diag(M)))` (the `diag` Matlab function converts a diagonal matrix to a vector of its diagonal entries, and vice versa). So, our code now uses only $m + 1$ 'true' matrix exponentials (listing 2.4). At this point, our matrix exponentials have almost been eliminated and the largest remaining bottleneck is almost certainly the matrix *multiplications* required for the propagation.

```
% precalculate pulse propagators; m total matrix exponentials
for pulse_point=1:m
    H_pulse = (c_x(pulse_point) * I_x) + (c_y(pulse_point) * I_y);
    U_pulse(m) = expm(-1j * (H_free + H_pulse) * t_pulse);
end

% loop over slices
for slce=1:n
    % calculate gradient propagators; n total matrix exponentials
    H_grad = I_z * G * z(slce);
    U_grad = expm(-1j * (H_free + H_grad) * t_grad);

    % loop over pulse points
    for point=1:m
        rho = U_pulse(m) * rho * U_pulse(m)';
        rho = U_grad * rho * U_grad';
    end
end
```

Listing 2.3: Rough structure of a slightly faster implementation of dPSYCHE.

We can cut this down by a factor of two simply by calculating the overall propagator

$$U_{\text{total}} = U_n \cdots U_2 U_1 \tag{2.49}$$

and then performing the propagation only at the very end:

$$\rho = U_{\text{total}} \rho_0 U_{\text{total}}^\dagger \tag{2.50}$$

instead of performing every individual step $\rho \rightarrow U_1 \rho_0 U_1^\dagger$. The final optimised code therefore resembles that in listing 2.4.

The performance of this handwritten code as compared to Spinach is summarised in table 2.1. In all cases, the spectra produced by the two methods were entirely equivalent. It should be noted that the handwritten code does not even utilise CPU parallelisation, whereas Spinach does. I investigated the possibility of parallelising the loop over slices (replacing the outer for in listing 2.4 with parfor): however, this in fact made the code *slower*, presumably due to overhead. This is a good thing: it means that parfor can be used in an external loop, e.g. for the parallel simulation of the dPSYCHE experiment on different spin systems.

```matlab
% precalculate propagator due to free evolution during gradient
% only 1 matrix exponential
U_free = expm(-1i * H_free * t_grad);

% precalculate pulse propagators; m total matrix exponentials
for pulse_point=1:m
    H_pulse = (c_x(pulse_point) * I_x) + (c_y(pulse_point) * I_y)
    U_pulse(m) = expm(-1j * (H_free + H_pulse) * t_pulse)
end

% loop over slices
for slce=1:n
    % initialise propagator for this slice
    U_slce = eye(2 ^ p);

    % calculate gradient propagators; no matrix exponentials required
    H_grad = I_z * G * z(slce);
    U_grad = U_free * diag(exp(diag(-1j * H_grad * t_grad)));

    % loop over pulse points
    for point=1:m
        U_slce = U_pulse(m) * U_slce;
        U_slce = U_grad * U_slce;
    end

    % perform propagation only at the end
    rho = U_slce * rho * U_slce';
end
```

Listing 2.4: Rough structure of a fast dPSYCHE implementation.

2.6.2 Optimisations and experimental evaluation

Spectrum-comparison cost function

As previously discussed, the fact that the dPSYCHE experiment can be very quickly simulated opens up the potential for entirely computational optimisation of the pulse sequence. For any arbitrary spin system, it is trivial to remove all the couplings *in silico* and simulate a pulse–acquire spectrum: this gives us a theoretically perfect pure shift spectrum. The simulated dPSYCHE experiment (on a system with couplings) can then be compared against this. The entire process is repeated using s different spin systems, and the cost function is defined as:

$$f_{\text{diff},2} = \frac{1}{s} \sum_{s} \left\| \frac{\mathbf{S}_{\text{re}} - c\mathbf{T}_{\text{re}}}{c\|\mathbf{T}_{\text{re}}\|} \right\|^2 \tag{2.51}$$

Number of spins	Number of couplings	Execution time (s)	
		Spinach	Handwritten
1	0	3.33	0.35
2	0	4.59	0.32
	1	6.22	0.32
3	0	9.90	0.43
	1	12.95	0.45
	2	31.86	0.47
	3	35.01	0.48
4	0	30.59	1.02
	1	38.63	0.99
	2	44.61	1.04
	3	365.04	1.52
	4	446.03	1.57
	5	521.72	1.57
	6	588.31	1.69

Table 2.1: Comparison of wall-clock times for dPSYCHE simulations. The dPSYCHE sequence used contained 15 pulses, each applied with a flip angle of 15° and a phase of 0°. Spin systems were generated pseudo-randomly. All timings were measured on a 2019 MacBook Pro with a 2.6 GHz 6-core Intel i7 CPU.

where S is the dPSYCHE spectrum, and T is the target spectrum. The prefactor c will be discussed later; for now I treat it as 1. This cost function appears superficially very similar to f_{diff} (discussed in § 2.4.1), and is based on the same principle that we want the spectra S and T to match one another, but there are several points of note:

- The spectrum S_{re} is not scaled down by its norm. This means that the sensitivity penalty no longer comes from the difference in the noise (as was previously the case), but rather directly from the difference in peak intensity. Since simulated spectra are noiseless, the original f_{diff} would not work here.

- The division of the entire cost function by $\|T_{\text{re}}\|$ is not important if only one spin system is being simulated as it is simply a constant factor. However, if more than one spin system is being simulated, $\|T_{\text{re}}\|$ differs from system to system and this factor helps to essentially normalise the contributions from each spin system.

- The norm in the cost function here is squared. Again, this makes no difference to the optimum if only one spin system is being investigated, because x^2 is strictly increasing for $x > 0$.* However, for multiple spin systems it makes sense to square the norm, as the

---

*It may affect the rate of convergence, but this is not something I tested.

largest deviations will be penalised more greatly: this means that a pure shift spectrum which works reasonably well across a wide range of spin systems will be prioritised over one which works perfectly well for some and fails badly for others.

I began by first checking how many t_1 increments (i.e. chunks) were required in the simulation to obtain reliable cost function values. If too few chunks are simulated, the resulting pure shift spectrum will have truncation artefacts, which are likely to mask artefacts from unwanted CTPs. The value of $f_{\text{diff},2}$ was thus tested with a wide variety of randomly chosen phases and angles, with the number of chunks set to 4, 8, and 16 (fig. 2.19).

./figures/pureshift/td1_cf.png

Figure 2.19: Comparison of $f_{\text{diff},2}$ values when simulated with different numbers of chunks. 16 chunks is assumed to be the 'gold standard'. **(a)** Correlation between 16-chunk and 8-chunk cost functions. The 'optimum' identified by both cost functions is plotted in green in the inset. **(b)** Correlation between 16-chunk and 4-chunk cost functions. The 'optima' identified by the 16- and 4-chunk cost functions are plotted in green and red respectively in the inset.

The 16-chunk and 8-chunk $f_{\text{diff},2}$ (fig. 2.19a) do in fact line up quite well. Notably, as the inset shows, they both agree on the 'best' candidate (note that this is not necessarily anywhere near perfect, since it was randomly generated). The 4-chunk $f_{\text{diff},2}$ also has the correct overall behaviour (fig. 2.19b). However, its ranking of the 'best' candidates is not very accurate: the 4-chunk cost function rates the red dot in the inset as the optimum, but that is only the 13th-best candidate when using the 16-chunk cost function. Ultimately, I decided to use the 4-chunk cost function for 'quick and dirty' optimisations, where only an approximate optimum was required. However, for anything requiring more accuracy, the 8-chunk cost function was used.

An optimisation was then carried out with a (rather arbitrarily chosen) setting of $m = 9$, i.e. nine hard pulses in the PSE. A total of $s = 20$ spin systems were used, matching the number of

CPU cores on the computer used for the optimisations: these were further subdivided into four two-spin systems, eight three-spin systems, and eight four-spin systems. The derivative-based BFGS algorithm was used to carry out the optimisation: this is a popular line search algorithm which uses an approximate Hessian to calculate the search direction at each iteration.[79,80] No lower or upper bounds were placed on the flip angles or phases: phases can obviously simply be wrapped to the region $[0, 2\pi)$, and in the simulations, the hard pulses were modelled as being instantaneous rotations, so their flip angles can also just be wrapped to $[0, 2\pi)$. (This would not be completely valid if realistic, finite pulses were used, since changing the flip angle would also change their duration.) This first optimisation yielded the following optimised parameters for the nine pulses:

$$\{\beta_i\} = \{118.6972°, 29.8400°, 107.4850°, 190.4788°,$$
$$138.4710°, 144.5939°, 18.9674°, 73.8900°, 130.6071°\} \quad (2.52) \quad \text{\{eq:dpsyche\_opt\_nosens}}$$
$$\{\phi_i\} = \{144.5641°, 173.3596°, 38.9878°, 146.3121°,$$
$$127.7346°, 7.5104°, 36.9805°, 110.2791°, 182.3894°\}. \quad (2.53) \quad \text{\{eq:dpsyche\_opt\_nosens}}$$

The fact that none of the flip angles exceeded 360° here provides some justification for not using bounds in the optimisation.

./figures/pureshift/dpsyche_nosens_vs_psyche.png

Figure 2.20: **(a)** dPSYCHE experiment acquired using the flip angles and phases in eqs. (2.52) and (2.53). The β hard pulses in the PSE were applied with an RF amplitude of **(b)** (Double-saltire) PSYCHE experiment acquired with $\beta = 20°$. *Data code:* `6A-211027`.

To evaluate the quality of the decoupling on a real sample, the dPSYCHE experiment was performed experimentally, and the results compared against a PSYCHE experiment (fig. 2.20). Firstly, it is worth pointing out that a pure shift spectrum (even if not a very good one) was obtained: this validates the form of the PSE and the optimisation approach used here, especially considering that the optimisation was not tailored towards this particular sample. The dPSYCHE experiment

clearly has much greater sensitivity than the PSYCHE experiment; however, the decoupling quality is extremely poor. The reason for this is likely because the optimisation is prioritising sensitivity too highly over purity, and ultimately stems from the factor c in eq. (2.51) which we have ignored until now. Since $c = 1$, the optimisation is essentially guiding the dPSYCHE experiment towards having *exactly the same sensitivity as a pulse–acquire experiment.*

Although this might be a nice idea in principle, it is not physically sensible: no pure shift method has sensitivity which is even close to that of a pulse–acquire experiment. It makes more sense to scale down the target spectrum by introducing a factor of $c < 1$ into the cost function (eq. (2.51)); the parameter c therefore represents the 'target sensitivity'. By changing the parameter c, we can control whether the optimisation emphasises sensitivity or purity more. (Note that this option was *not* available to us in the experimental JRSE-based optimisations in § 2.4.)

A series of new optimisations were therefore run, with c ranging from 0.2 to 1 (table 2.2). The 4-chunk cost function was used, and the maximum number of function evaluations capped at 5000. Each optimisation was run 10 times with a different starting seed, and the best of the 10 results chosen for further evaluation (table 2.2). The resulting spectra (fig. 2.21) show that adjusting c has the desired effect: larger values lead to greater sensitivity and lower purity, and vice versa.

In this spectrum of andrographolide, the 3.5 ppm to 5 ppm region (blue inset) is an 'easier' region to decouple: there are fewer couplings here and all spin systems are firmly within the weak coupling regime. The 1.5 ppm to 2.8 ppm region (orange inset) is 'more difficult' to decouple, especially the two peaks at 2.5 ppm, which are mutually strongly coupled. The dPSYCHE spectrum with $c = 0.4$ appeared to be a good compromise between purity and sensitivity: its sensitivity was higher than that of the original (20° flip angle) PSYCHE experiment. Furthermore, it provided good decoupling in the 'easier' deshielded region and somewhat acceptable performance in the shielded region, with the notable exception of the strongly coupled peaks at 2.5 ppm.

I therefore ran a longer optimisation using the same starting point and with no limit on the number of function evaluations, which successfully lowered the cost function value by twofold (the last entry in table 2.2). The pure shift spectrum obtained using these optimised pulses is shown in fig. 2.22. The decoupling quality in both regions is comparable to that in the PSYCHE spectrum, again with the exception of the strongly coupled peaks at 2.5 ppm.

To make the dPSYCHE experiment more robust towards strong coupling, a TSE version of the sequence was also written and tested (fig. 2.23). This did indeed improve the decoupling at 2.5 ppm, as expected. However, although the TSE-dPSYCHE version still retains its *overall* sensitivity advantage over TSE-PSYCHE (especially evident in the deshielded region), this is not true of every peak: the two peaks at 1.65 and 1.70 ppm seem to have decreased intensities
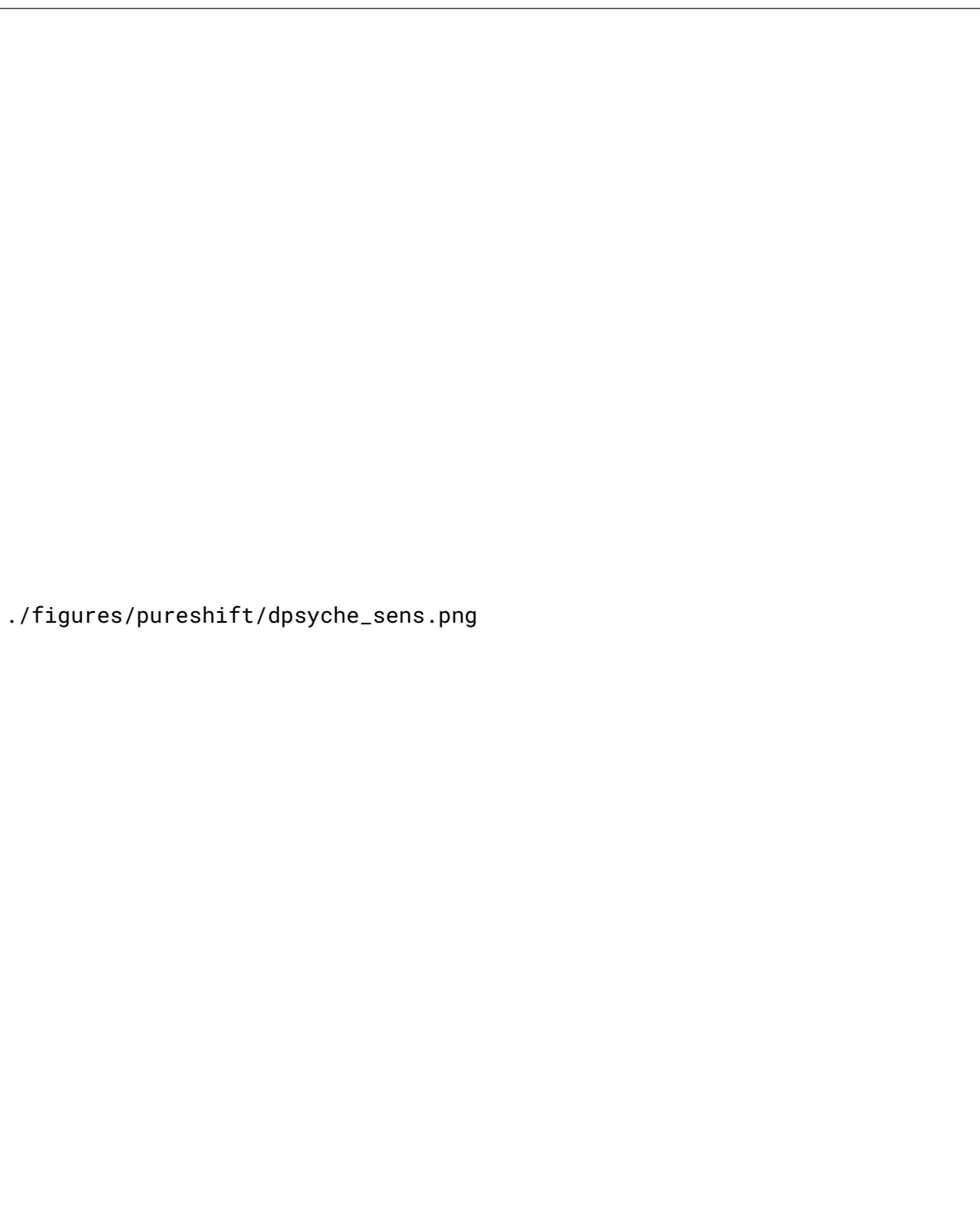
Figure 2.21: **(a)** dPSYCHE, $c = 1$. **(b)** dPSYCHE, $c = 0.8$. **(c)** dPSYCHE, $c = 0.6$. **(d)** dPSYCHE, $c = 0.4$. **(e)** dPSYCHE, $c = 0.2$. **(f)** Double-saltire PSYCHE with $\beta = 20°$. All spectra and insets are plotted to scale to allow for sensitivity comparisons. *Data code:* 6A-211231.

c	Flip angles (°)	Phases (°)	$f_{\text{diff},2}$
1	59.8813, 96.0748, 111.5862, 118.7285, 144.701, 176.9773, 29.2866, 40.0658, 63.8237	355.773, 81.741, 99.8752, 81.6675, 337.0056, 150.7004, 105.9666, 317.9979, 27.7897	0.0404
0.8	81.9461, 65.311, 90.3488, 106.6388, 73.3462, 196.7857, 51.791, 34.8188, 53.9506	329.8571, 60.3564, 137.3929, 68.5286, 340.74, 126.29, 64.4601, 145.4714, 27.3019	0.0321
0.6	53.1313, 82.2547, 88.6093, 161.9291, 83.462, 161.3548, 14.2976, 66.2199, 53.9709	347.2835, 59.5518, 68.072, 113.5358, 34.5537, 156.191, 268.7641, 302.7427, 16.29	0.0250
0.4	77.2998, 127.7274, 87.6663, 104.6371, 99.6474, 168.8171, 8.8569, 52.7865, 58.1408	342.2787, 47.7526, 76.4114, 97.3304, 14.2178, 163.9513, 94.2575, 280.0273, 16.0971	0.0271
0.2	120.6613, 107.6712, 84.0427, 133.5377, 82.1999, 223.122, 41.1617, 41.9398, 12.016	347.2051, 79.4503, 109.8796, 83.5017, 345.4284, 133.8355, 66.4118, 201.0041, 4.4419	0.0261
0.4*	92.4395, 133.2136, 38.9704, 34.9182, 56.0256, 57.4097, 31.5916, 140.1088, 128.7125	62.036, 16.411, 319.5634, 128.4443, 49.7357, 328.5103, 210.6498, 44.0123, 327.4517	0.0108

tbl:dpsyche_sens

Table 2.2: Results of dPSYCHE optimisations for different sensitivities. Note that since the cost function depends on the value of c, the exact value of $f_{\text{diff},2}$ for these optimisations cannot be compared to one another; they are only presented here for completeness. The final entry, labelled with an asterisk, was run with no limit on the number of function evaluations (this is discussed further in the text).

in the TSE-dPSYCHE experiment. The reason for this is not fully clear. One could say that the optimised pulses are not likely work equally well on *all* combinations of chemical shifts and couplings, and these peaks may simply fall into one of the less effective regions; but in the (non-TSE) dPSYCHE experiment (fig. 2.22a), these distortions in intensity are not observed. One possible conclusion is that some of the intensity in the non-TSE experiment in fact stems from artefacts which are not fully suppressed: this may also explain the slight broadening at the base of the peaks in fig. 2.22a.

State-transfer cost function

The optimisations conducted so far have been based on directly evaluating the simulated pure shift spectrum. However, since these optimisations are conducted in a purely theoretical manner, it is possible to simply calculate the effect of the PSE on each input state to determine its quality. We would want to maximise the degree of desired state transfer (which leads to the pure shift signal), and minimise the degree of unwanted state transfers (which lead to artefacts). This would
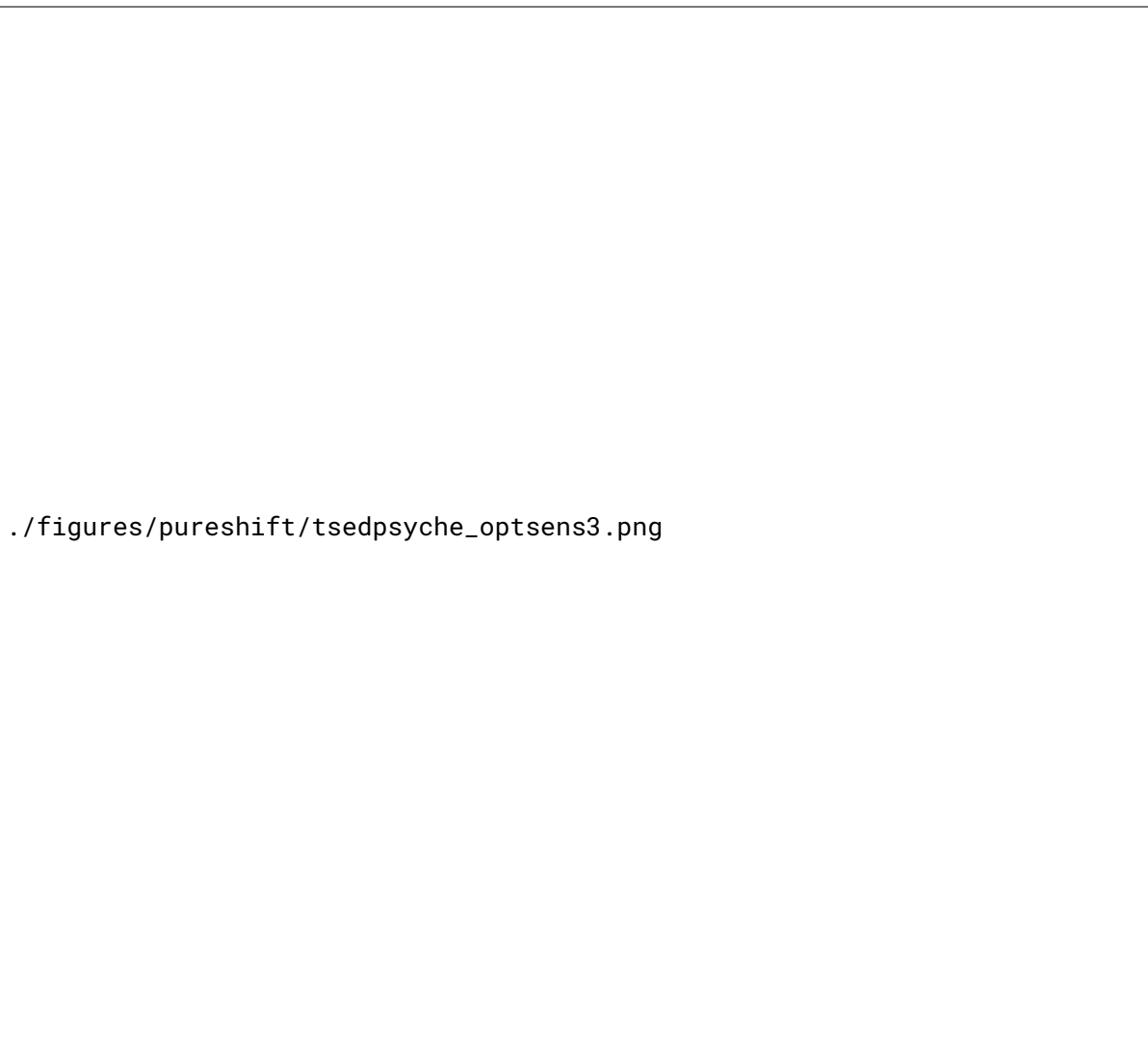
./figures/pureshift/dpsyche_optsens3.png

Figure 2.22: **(a)** Fully optimised dPSYCHE experiment with $c = 0.4$. **(b)** Double-saltire PSYCHE with $\beta = 20°$. *Data code:* 6A-211231.

be a more direct way of evaluating the PSE.

We can split the possible state transfers up into several categories:

1. desired (e.g. $I_{1+}I_{2\alpha} \rightarrow I_{1-}I_{2\alpha}$)

2. undesired, but can be dephased by CTP gradients (e.g. $I_{1+}I_{2\alpha} \rightarrow I_{1+}I_{2\alpha}$)

3. undesired, but can be suppressed by the TSE element (e.g. $I_{1+}I_{2\alpha} \rightarrow I_{1\alpha}I_{2-}$)

4. undesired, but survive even with the TSE element (e.g. $I_{1+}I_{2\alpha} \rightarrow I_{1-}I_{2\beta}$)

For a TSE-dPSYCHE experiment, we only need to consider items (1) and (4); without the TSE addition, we would additionally need to take item (3) into account. These state transfer coefficients would also have to be summed over all possible input states: for an *n*-spin system, there are

Figure 2.23: **(a)** Fully optimised TSE-dPSYCHE experiment with $c = 0.4$. **(b)** Double-saltire TSE-PSYCHE with $\beta = 20°$. *Data code:* 7A-220129.

$n \cdot 2^{n-1}$ possible input states (n possible spins which could be active, and 2^{n-1} permutations of passive spin states). The cost function would then be constructed as a linear combination of these two or three terms, where the coefficients serve a similar function to the parameter c in the spectrum-comparison cost function (eq. (2.51)) in that they control the balance between sensitivity and purity.

Table comparing fspec and fstate?

Unfortunately, even though all of the code for efficient (parallelised) computation of this cost function was written, I did not have the time to actually perform optimisations using this cost function and to experimentally validate the results. This is a slight disappointment to me, as the initial results shown in this section have been quite promising, and it is likely that the state

transfer-based optimisations would have improved this even further. However, even from just the results obtained so far, it is clear that the interleaved pulses and gradients used in the dPSYCHE PSE form a reasonable *ansatz* which can yield pure shift spectra which are almost comparable to the PSYCHE method.

2.7 Ultrafast PSYCHE-iDOSY

In the final section of this chapter, I turn to something entirely different: the combination of pure shift diffusion NMR with ultrafast acquisition. This work was done in collaboration with Jean-Nicolas Dumez (University of Nantes): the original project idea was first conceived and implemented there. Unfortunately, the results we obtained at Oxford were not promising enough to drive the project further, especially in light of time constraints. However, for the sake of completeness, I describe the overall concept as well as these results in this section.

Figure 2.24: **(a)** Basic stimulated echo DOSY experiment. To acquire the diffusion dimension, the amplitudes of gradients with arrows inside are incremented. Δ indicates the diffusion delay. **(b)** PSYCHE-iDOSY experiment. τ is set to $1/(4 \cdot T_{\text{chunk}})$, as before. **(c)** Ultrafast DOSY experiment. The EPSI acquisition block is highlighted in orange, consisting of a prephasing gradient followed by detection in the presence of alternating gradients. **(d)** Ultrafast PSYCHE-iDOSY experiment. Note the use of unidirectional chirps rather than saltire pulses.

I begin with a brief overview of diffusion NMR;[81] this topic will also be covered in some detail in § 3.4.10. Figure 2.24a shows a typical 2D stimulated echo DOSY experiment, where the indirect (diffusion) dimension involves the incrementation of gradient amplitudes rather than

an evolution delay. For each gradient amplitude, one time-domain signal is recorded. Molecular diffusion during a delay placed between a pair of gradients leads to attenuation of the signal, as the spatially-dependent phase imparted by the first gradient is not perfectly refocused by the second. This attenuation is described by the Stejskal–Tanner equation,[82,83] which in its simplest form is:

$$I(G) = I(0) \exp\left[-(\gamma\delta G)^2 D\Delta'\right]. \tag{2.54}$$

{eq:stejskal_tanner}

Here, $I(G)$ represents the signal intensity when measured with a gradient amplitude of G; γ is the magnetogyric ratio, δ is the duration of the bracketing gradients, D the diffusion coefficient, and Δ' a 'corrected' diffusion delay. The exact correction required depends on the shapes of the gradients used. By measuring the signal intensity I for at least two different values of G, the diffusion coefficient D can be estimated.[*]

The fact that different molecules have different diffusion coefficients, and thus different attenuation profiles, can be used to separate mixtures of molecules through the basic DOSY experiment. However, when signals from different species overlap in the ^{1}H spectrum, (as is often the case in mixtures), it is not possible to cleanly extract the separate peak intensities, resulting in poor resolution in the diffusion dimension. There are several ways to solve this issue: for example, peaks can be resolved using another chemical shift dimension in a 3D experiment.[84–88] A slightly less time-consuming option is pure shift NMR. The first pure shift diffusion experiments used either the 45° projection of a 2DJ spectrum,[89] or the Zangger–Sterk PSE:[29,90,91] in both cases, improvements in the resolution of diffusion coefficients were reported. The PSYCHE-iDOSY experiment[57] (fig. 2.24b) improved upon these, much in the same way that PSYCHE itself improved on existing pure shift methods. The 'i' refers to the fact that the diffusion delay is *internal* to the sequence, i.e. it is simply added in the middle of the PSYCHE element, which (using the instantaneous flip approximation) can itself be thought of as a spatially parallel stimulated echo. This avoids the need to add an entirely separate stimulated echo at the beginning or end of the sequence.

While the addition of a pure shift dimension is less expensive compared to a full chemical shift dimension in terms of time, the fact remains that the PSYCHE-iDOSY is a (pseudo)-3D experiment. One way to shorten this is to use spatial encoding techniques to collapse one dimension, specifically the diffusion dimension.[92] Two separate steps are required for this: firstly, a gradient whose amplitude varies across the sample must be applied (the 'encoding' step), and then an imaging acquisition technique must be used to read out the signal in each slice of the sample (the 'detection' step). This was first done by Loening et al.,[93] where the encoding was performed using the field generated by a z^2 shim coil. The readout was then performed by simply

---

[*]As will be discussed in § 3.4.10, this should really be an *apparent* diffusion coefficient as there are various other factors which can affect the intensity, notably convection.

acquiring the FID in the presence of a weak gradient, such that the peak shapes directly reflect the distribution of signal intensities across the sample. Later, Thrippleton et al.[94] introduced the (by now familiar) chirp–gradient combination for spatial encoding: since spins in different slices are inverted at different times, the total gradient area applied in each slice is different. In later work by the groups of Frydman[95] and Dumez,[96,97] the spatial encoding of the diffusion attenuation is still accomplished using the very same chirp–gradient combination. However, the detection is accomplished using the echo-planar spectroscopic imaging (EPSI) acquisition technique,[98,99] much like in ultrafast 2D NMR (fig. 2.24c).[58–60,62,100–102]

Unsurprisingly, the aim in this section is to unite the PSYCHE-iDOSY and ultrafast DOSY techniques to form an ultrafast PSYCHE-iDOSY experiment. This would yield PSYCHE-iDOSY spectra in a much reduced time, at the cost of sensitivity. The resulting pulse sequence is shown in fig. 2.24d. The EPSI acquisition is used to collapse the diffusion dimension, not the PSYCHE chunking dimension.* One benefit of this is that only one PSYCHE chunk needs to be acquired at a time, circumventing the need for long EPSI detection periods (which can cause spectrometer damage). Note also that it is mandatory to use unidirectional chirps in the PSYCHE PSE: in the original PSYCHE-iDOSY, these pulses were used only for homonuclear decoupling, and thus saltire pulses were acceptable (indeed, superior). However, in the ultrafast version, the PSE is also responsible for creating the requisite spatial encoding of gradient areas. Using saltire pulses here would lead to an undesired 'double' encoding, yielding data which cannot be processed correctly.

The sequence itself was written and evaluated by Corentin Jacquemmoz and Jean-Nicolas Dumez at the University of Nantes, on a concentrated (1 M) sample of ethanol in D_2O. Their results are shown in figs. 2.25a to 2.25c. When I later tried to reproduce these results, I additionally used the POISE routine described in § 3.4.6 to optimise the amplitude ratio between the positive and negative gradients during the EPSI acquisition (without optimisation, the results obtained were even poorer); my results are shown in figs. 2.25d to 2.25f. The data processing used to generate these figures was written by me,† and broadly consists of the following steps: reshaping of the EPSI raw data, concatenation of PSYCHE chunks, and Fourier transformation in both dimensions.‡ For simplicity, the data points acquired during the negative gradients is discarded.

In principle, the Fourier transformed (z, δ) plots should reveal a diffusion profile similar to that

---

*The other option would require an ultrafast PSYCHE experiment, which—to date—has not been developed.

†The Nantes team have a more complete Matlab package for this, which goes several steps further than that shown here and includes features such as phase correction and fitting of the diffusion profiles to various (though not yet fully appropriate) Stejskal–Tanner equations. However, these were not necessary here as the project never got to that stage, and I preferred to use Python.

‡As discussed in Frydman et al.,[60] the k-domain in ultrafast NMR is directly proportional to the indirect-dimension frequency domain. So, to obtain the diffusion profile—which varies with space, i.e. z—a Fourier transform along this axis is required.

Figure 2.25: **(a)–(c)** EPSI PSYCHE-iDOSY data obtained by Corentin Jacquemmoz and Jean-Nicolas Dumez at the University of Nantes. The three plots respectively show the 2D raw (k, t_2) data (after PSYCHE processing has been carried out); the Fourier transformed (z, δ) data; and the individual diffusion profiles for each peak. **(d)–(f)** The equivalent data which I recorded in Oxford. The central peak corresponds to HDO; the Oxford sample used was drier and thus it is less intense in (e) compared to (b). *Data code:* 6E-210426.

in Guduff et al.[96] This is the case for the Nantes data; in fact, it was possible to process this further to obtain a conventional 2D DOSY spectrum, where the diffusion coefficient for each component is extracted and plotted. For the Oxford data, although the general *form* of the curve is correct (in that there is a generally decreasing pattern), there are clearly 'spikes' in the (z, δ) diffusion profiles.

My current best hypothesis is that these spikes are artefacts from unwanted CTPs which are ordinarily suppressed through spatial averaging, but are instead being refocused by the gradients during the EPSI acquisition. This is supported by the fact that the Nantes data was acquired on a microimaging probe equipped with triaxial gradients, which allowed CTP gradients to be applied along the *x*- and *y*-axes (note that the PSYCHE gradient must still be applied along the *z*-axis). Naturally, any artefacts dephased by these cannot be refocused by the *z*-gradients in the EPSI block. On the other hand, the Oxford data was acquired on a Prodigy cryoprobe with only *z*-gradients.

The intensity of these 'spike' artefacts can, in fact, be controlled by varying other acquisition parameters. For example, increasing the EPSI gradient amplitude leads to increased artefacts (figs. 2.26a and 2.26b): this lends credence to the hypothesis above that the artefacts arise from refocused CTPs. Notice also the appearance of signals at $k \neq 0$: this should not happen because in ultrafast experiments, the *k*-axis is proportional to the evolution frequency as a function of *z* (i.e. indirect-dimension frequencies in a typical 2D experiment). In a diffusion experiment, however, there is no frequency modulation in the indirect or spatial dimension, only amplitude modulation arising from diffusion attenuation; so, all signals should fall along $k = 0$. In principle, the EPSI gradient could instead be reduced, but this has the drawback of lowering the resolution in the diffusion dimension. Alternatively, when the PSYCHE gradient is increased, the artefacts seem to be reduced (figs. 2.26c and 2.26d). However, this cannot be varied too much as the PSYCHE gradients are also responsible for the diffusion encoding (the value of *g* in the Stejskal–Tanner equation are effectively derived from this).

Another possible reason for the artefacts is a potentially poorer B_1 homogeneity on the Oxford instrument. However, a simple pulse–EPSI experiment (fig. 2.27) shows that the B_1 spatial profile, though not perfect, is relatively uniform.

Curiously, fig. 2.25d shows that in the Oxford data, there is a progressive 'shifting' along the *k*-axis in each PSYCHE chunk. (The POISE optimisation in § 3.4.6 was used to correct for the drifting *within* each chunk, but cannot be applied to the overall drift after the concatenation of chunks.) One possible explanation for this is perhaps lingering effects from gradients applied during the pulse sequence, which have more time to dissipate when t_1 is longer. This, however, does not have an appreciable impact on the data: it can be crudely corrected by circularly shifting the data along the *k*-axis by an appropriate amount, and Fourier transformation of the resulting data

Figure 2.26: **(a)–(b)** The same as in figs. 2.25d and 2.25f, but with the EPSI acquisition gradient increased to 32% (from 24% in the original). *Data code:* `6E-210426`. **(c)–(d)** The same as in figs. 2.25d and 2.25f, but with the PSYCHE gradient increased to 5% (from 3% in the original). *Data code:* `6E-210505`.

yielded effectively the same results.

All in all, it appears that the fundamental idea behind the ultrafast PSYCHE-iDOSY experiment is sound: the Nantes data is an excellent proof-of-principle. However, the implementation of the sequence almost certainly needs to be optimised in order for high-quality data to be extracted. An important subsequent step would then be to derive the appropriate form of the Stejskal–Tanner equation for extracting diffusion coefficients from the data. Sadly, I simply did not quite have the time to pursue this in further detail.

2.8 References

Zangger2015PNMRS

(1)   Zangger, K. Pure shift NMR. *Prog. Nucl. Magn. Reson. Spectrosc.* **2015**, *86-87*, 1–20, DOI: `10.1016/j.pnmrs.2015.02.002`.

./figures/pureshift/zg_epsi.png

Figure 2.27: **(a)** Pulse–EPSI pulse sequence. The variation of the peak intensity along the z-axis directly corresponds to the B_1 spatial profile. **(b)** The resulting data after Fourier transformation in both dimensions ($k \leftrightarrow z$ and $t_2 \leftrightarrow \delta$). *Data code:* 6E-210426.

Castanar2017MRC   (2)   Castañar, L. Pure shift ^{1}H NMR: what is next? *Magn. Reson. Chem.* **2017**, *55*, 47–53, DOI: 10.1002/mrc.4545.

Keeler2010   (3)   Keeler, J., *Understanding NMR Spectroscopy*, 2nd ed.; Wiley: Chichester, U.K., 2010.

Thrippleton2005JMR   (4)   Thrippleton, M. J.; Edden, R. A. E.; Keeler, J. Suppression of strong coupling artefacts in J-spectra. *J. Magn. Reson.* **2005**, *174*, 97–109, DOI: 10.1016/j.jmr.2005.01.012.

Griesinger1986JCP   (5)   Griesinger, C.; Sørensen, O. W.; Ernst, R. R. Correlation of connected transitions by two-dimensional NMR spectroscopy. *J. Chem. Phys.* **1986**, *85*, 6837–6852, DOI: 10.1063/1.451421.

Aue1976JCP   (6)   Aue, W. P.; Karhan, J.; Ernst, R. R. Homonuclear broad band decoupling and two-dimensional J-resolved NMR spectroscopy. *J. Chem. Phys.* **1976**, *64*, 4226–4227, DOI: 10.1063/1.431994.

Xu1991JMR   (7)   Xu, P.; Wu, X.-L.; Freeman, R. Broadband-decoupled proton spectroscopy. *J. Magn. Reson.* **1991**, *95*, 132–148, DOI: 10.1016/0022-2364(91)90329-r.

Nuzillard1996JMRSA   (8)   Nuzillard, J.-M. Time-Reversal of NMR Signals by Linear Prediction. Application to Phase-Sensitive Homonuclear J-Resolved Spectroscopy. *J. Magn. Reson., Ser. A* **1996**, *118*, 132–135, DOI: 10.1006/jmra.1996.0020.

Simova1997JMR   (9)   Simova, S.; Sengstschmid, H.; Freeman, R. Proton Chemical-Shift Spectra. *J. Magn. Reson.* **1997**, *124*, 104–121, DOI: 10.1006/jmre.1996.1001.

Pell2007JMR   (10)   Pell, A. J.; Keeler, J. Two-dimensional J-spectra with absorption-mode lineshapes. *J. Magn. Reson.* **2007**, *189*, 293–299, DOI: 10.1016/j.jmr.2007.09.002.

Foroozandeh2015CC   (11)   Foroozandeh, M.; Adams, R. W.; Kiraly, P.; Nilsson, M.; Morris, G. A. Measuring couplings in crowded NMR spectra: pure shift NMR with multiplet analysis. *Chem. Commun.* **2015**, *51*, 15410–15413, DOI: 10.1039/c5cc06293d.

Griesinger1985JACS

(12) Griesinger, C.; Soerensen, O. W.; Ernst, R. R. Two-dimensional correlation of connected NMR transitions. *J. Am. Chem. Soc.* **1985**, *107*, 6394–6396, DOI: 10.1021/ja00308a042.

Sorensen1985JACS

(13) Sørensen, O. W.; Griesinger, C.; Ernst, R. R. Time reversal of the evolution under scalar spin-spin interactions in NMR. Application for ω_1 decoupling in two-dimensional NOE spectroscopy. *J. Am. Chem. Soc.* **1985**, *107*, 7778–7779, DOI: 10.1021/ja00311a101.

Oschkinat1986JMR

(14) Oschkinat, H.; Pastore, A.; Pfändler, P.; Bodenhausen, G. Two-dimensional correlation of directly and remotely connected transitions by z-filtered COSY. *J. Magn. Reson.* **1986**, *69*, 559–566, DOI: 10.1016/0022-2364(86)90176-9.

Pell2007MRC

(15) Pell, A. J.; Edden, R. A. E.; Keeler, J. Broadband proton-decoupled proton spectra. *Magn. Reson. Chem.* **2007**, *45*, 296–316, DOI: 10.1002/mrc.1966.

Moutzouri2020ACIE

(16) Moutzouri, P.; Paruzzo, F. M.; Simões de Almeida, B.; Stevanato, G.; Emsley, L. Homonuclear Decoupling in ^{1}H NMR of Solids by Remote Correlation. *Angew. Chem., Int. Ed.* **2020**, *59*, 6235–6238, DOI: 10.1002/anie.201916335.

Bruschweiler2004JCP

(17) Brüschweiler, R.; Zhang, F. Covariance nuclear magnetic resonance spectroscopy. *J. Chem. Phys.* **2004**, *120*, 5253–5260, DOI: 10.1063/1.1647054.

Zhang2004JACS

(18) Zhang, F.; Brüschweiler, R. Indirect Covariance NMR Spectroscopy. *J. Am. Chem. Soc.* **2004**, *126*, 13180–13181, DOI: 10.1021/ja047241h.

Jaeger2014ARNMRS

(19) Jaeger, M.; Aspers, R. L. E. G. Covariance NMR and Small Molecule Applications. *Annu. Rep. NMR Spectrosc.* **2014**, *83*, 271–349, DOI: 10.1016/B978-0-12-800183-7.00005-8.

Morris2010JACS

(20) Morris, G. A.; Aguilar, J. A.; Evans, R.; Haiber, S.; Nilsson, M. True Chemical Shift Correlation Maps: A TOCSY Experiment with Pure Shifts in Both Dimensions. *J. Am. Chem. Soc.* **2010**, *132*, 12770–12772, DOI: 10.1021/ja1039715.

Aguilar2012ACIE

(21) Aguilar, J. A.; Colbourne, A. A.; Cassani, J.; Nilsson, M.; Morris, G. A. Decoupling Two-Dimensional NMR Spectroscopy in Both Dimensions: Pure Shift NOESY and COSY. *Angew. Chem., Int. Ed.* **2012**, *51*, 6460–6463, DOI: 10.1002/anie.201108888.

Foroozandeh2014JACS

(22) Foroozandeh, M.; Adams, R. W.; Nilsson, M.; Morris, G. A. Ultrahigh-Resolution Total Correlation NMR Spectroscopy. *J. Am. Chem. Soc.* **2014**, *136*, 11867–11869, DOI: 10.1021/ja507201t.

Lupulescu2012JMR

(23) Lupulescu, A.; Olsen, G. L.; Frydman, L. Toward single-shot pure-shift solution ^{1}H NMR by trains of BIRD-based homonuclear decoupling. *J. Magn. Reson.* **2012**, *218*, 141–146, DOI: 10.1016/j.jmr.2012.02.018.

Meyer2013ACIE

(24) Meyer, N. H.; Zangger, K. Simplifying Proton NMR Spectra by Instant Homonuclear Broadband Decoupling. *Angew. Chem., Int. Ed.* **2013**, *52*, 7143–7146, DOI: 10.1002/anie.201300129.

Mauhart2015JMR   (25)   Mauhart, J.; Glanzer, S.; Sakhaii, P.; Bermel, W.; Zangger, K. Faster and cleaner real-time pure shift NMR experiments. *J. Magn. Reson.* **2015**, *259*, 207–215, DOI: `10.1016/j.jmr .2015.08.011`.

Kiraly2018MRC   (26)   Kiraly, P.; Nilsson, M.; Morris, G. A. Practical aspects of real-time pure shift HSQC experiments. *Magn. Reson. Chem.* **2018**, *56*, 993–1005, DOI: `10.1002/mrc.4704`.

Donovan2014ACIE   (27)   Donovan, K. J.; Frydman, L. HyperBIRD: A Sensitivity-Enhanced Approach to Collecting Homonuclear-Decoupled Proton NMR Spectra. *Angew. Chem., Int. Ed.* **2014**, n/a–n/a, DOI: `10.1002/anie.201407869`.

Taylor2021MRC   (28)   Taylor, D. A.; Natrajan, L. S.; Nilsson, M.; Adams, R. W. SABRE-enhanced real-time pure shift NMR spectroscopy. *Magn. Reson. Chem.* **2021**, *59*, 1244–1252, DOI: `10.1002/mrc .5206`.

Aguilar2010ACIE   (29)   Aguilar, J. A.; Faulkner, S.; Nilsson, M.; Morris, G. A. Pure Shift ^{1}H NMR: A Resolution of the Resolution Problem? *Angew. Chem., Int. Ed.* **2010**, *49*, 3901–3903, DOI: `10.1002 /anie.201001107`.

Moutzouri2017CC   (30)   Moutzouri, P.; Chen, Y.; Foroozandeh, M.; Kiraly, P.; Phillips, A. R.; Coombes, S. R.; Nilsson, M.; Morris, G. A. Ultraclean pure shift NMR. *Chem. Commun.* **2017**, *53*, 10188–10191, DOI: `10.1039/c7cc04423b`.

Zangger1997JMR   (31)   Zangger, K.; Sterk, H. Homonuclear Broadband-Decoupled NMR Spectra. *J. Magn. Reson.* **1997**, *124*, 486–489, DOI: `10.1006/jmre.1996.1063`.

Garbow1982CPL   (32)   Garbow, J. R.; Weitekamp, D. P.; Pines, A. Bilinear rotation decoupling of homonuclear scalar interactions. *Chem. Phys. Lett.* **1982**, *93*, 504–509, DOI: `10.1016/0009-2614(82 )83229-6`.

Aguilar2011ACIE   (33)   Aguilar, J. A.; Nilsson, M.; Morris, G. A. Simple Proton Spectra from Complex Spin Systems: Pure Shift NMR Spectroscopy Using BIRD. *Angew. Chem., Int. Ed.* **2011**, *50*, 9716–9717, DOI: `10.1002/anie.201103789`.

Foroozandeh2014ACIE   (34)   Foroozandeh, M.; Adams, R. W.; Meharry, N. J.; Jeannerat, D.; Nilsson, M.; Morris, G. A. Ultrahigh-Resolution NMR Spectroscopy. *Angew. Chem., Int. Ed.* **2014**, *53*, 6990–6992, DOI: `10.1002/anie.201404111`.

Foroozandeh2018CEJ   (35)   Foroozandeh, M.; Morris, G. A.; Nilsson, M. PSYCHE Pure Shift NMR Spectroscopy. *Chem. Eur. J.* **2018**, *24*, 13988–14000, DOI: `10.1002/chem.201800524`.

Foroozandeh2020JMR   (36)   Foroozandeh, M. Spin dynamics during chirped pulses: applications to homonuclear decoupling and broadband excitation. *J. Magn. Reson.* **2020**, *318*, 106768, DOI: `10.1016 /j.jmr.2020.106768`.

Kupce1995JMRSB   (37)   Kupce, E.; Boyd, J.; Campbell, I. D. Short Selective Pulses for Biochemical Applications. *J. Magn. Reson., Ser. B* **1995**, *106*, 300–303, DOI: `10.1006/jmrb.1995.1049`.

Giraud2010ACIE (38) Giraud, N.; Béguin, L.; Courtieu, J.; Merlet, D. Nuclear Magnetic Resonance Using a Spatial Frequency Encoding: Application to J-Edited Spectroscopy along the Sample. *Angew. Chem., Int. Ed.* **2010**, *49*, 3481–3484, DOI: 10.1002/anie.200907103.

Gubensak2014CC (39) Gubensäk, N.; Fabian, W. M. F.; Zangger, K. Disentangling scalar coupling patterns by real-time SERF NMR. *Chem. Commun.* **2014**, *50*, 12254–12257, DOI: 10.1039/c4cc05892e.

Mishra2017JMR (40) Mishra, S. K.; Suryaprakash, N. Pure shift edited ultra high resolution NMR spectrum with complete eradication of axial peaks and unwanted couplings. *J. Magn. Reson.* **2017**, *279*, 74–80, DOI: 10.1016/j.jmr.2017.04.014.

Buchberger2018MRC (41) Buchberger, K.; Walenta, M.; Zangger, K. Extracting unresolved coupling constants from complex multiplets by a real-time J-upscaled SERF experiment. *Magn. Reson. Chem.* **2018**, *56*, 934–940, DOI: 10.1002/mrc.4699.

Uhrin1993JMRSA (42) Uhrin, D.; Liptaj, T.; Kover, K. E. Modified BIRD Pulses and Design of Heteronuclear Pulse Sequences. *J. Magn. Reson., Ser. A* **1993**, *101*, 41–46, DOI: 10.1006/jmra.1993.1005.

Sakhaii2009JMR (43) Sakhaii, P.; Haase, B.; Bermel, W. Experimental access to HSQC spectra decoupled in all frequency dimensions. *J. Magn. Reson.* **2009**, *199*, 192–198, DOI: 10.1016/j.jmr.2009.04.016.

Paudel2013ACIE (44) Paudel, L.; Adams, R. W.; Király, P.; Aguilar, J. A.; Foroozandeh, M.; Cliff, M. J.; Nilsson, M.; Sándor, P.; Waltho, J. P.; Morris, G. A. Simultaneously Enhancing Spectral Resolution and Sensitivity in Heteronuclear Correlation NMR Spectroscopy. *Angew. Chem., Int. Ed.* **2013**, *52*, 11616–11619, DOI: 10.1002/anie.201305709.

Reinsperger2014JMR (45) Reinsperger, T.; Luy, B. Homonuclear BIRD-decoupled spectra for measuring one-bond couplings with highest resolution: CLIP/CLAP-RESET and constant-time-CLIP/CLAP-RESET. *J. Magn. Reson.* **2014**, *239*, 110–120, DOI: 10.1016/j.jmr.2013.11.015.

Nolis2019JMR_psHSQC (46) Nolis, P.; Motiram-Corral, K.; Pérez-Trujillo, M.; Parella, T. Broadband homodecoupled time-shared ^{1}H–^{13}C and ^{1}H–^{15}N HSQC experiments. *J. Magn. Reson.* **2019**, *298*, 23–30, DOI: 10.1016/j.jmr.2018.11.005.

Singh2020JMR (47) Singh, U.; Bhattacharya, S.; Baishya, B. Pure shift HMQC: Resolution and sensitivity enhancement by bilinear rotation decoupling in the indirect and direct dimensions. *J. Magn. Reson.* **2020**, *311*, 106684, DOI: 10.1016/j.jmr.2020.106684.

Zwahlen1997JACS (48) Zwahlen, C.; Legault, P.; Vincent, S. J. F.; Greenblatt, J.; Konrat, R.; Kay, L. E. Methods for Measurement of Intermolecular NOEs by Multinuclear NMR Spectroscopy: Application to a Bacteriophage λ N-Peptide/boxBRNA Complex. *J. Am. Chem. Soc.* **1997**, *119*, 6711–6721, DOI: 10.1021/ja970224q.

Kupce2007JMR (49) Kupče, E.; Freeman, R. Compensated adiabatic inversion pulses: Broadband INEPT and HSQC. *J. Magn. Reson.* **2007**, *187*, 258–265, DOI: 10.1016/j.jmr.2007.05.009.

Thrippleton2003ACIE   (50)   Thrippleton, M. J.; Keeler, J. Elimination of Zero-Quantum Interference in Two-Dimensional NMR Spectra. *Angew. Chem., Int. Ed.* **2003**, *42*, 3938–3941, DOI: 10.1002/anie.200351947.

Timari2015CEJ   (51)   Timári, I.; Szilágyi, L.; Kövér, K. E. PSYCHE CPMG–HSQMBC: An NMR Spectroscopic Method for Precise and Simple Measurement of Long-Range Heteronuclear Coupling Constants. *Chem. Eur. J.* **2015**, *21*, 13939–13942, DOI: 10.1002/chem.201502641.

Koos2016ACIE   (52)   Koos, M. R. M.; Kummerlöwe, G.; Kaltschnee, L.; Thiele, C. M.; Luy, B. CLIP-COSY: A Clean In-Phase Experiment for the Rapid Acquisition of COSY-type Correlations. *Angew. Chem., Int. Ed.* **2016**, *55*, 7655–7659, DOI: 10.1002/anie.201510938.

Sinnaeve2016ACIE   (53)   Sinnaeve, D.; Foroozandeh, M.; Nilsson, M.; Morris, G. A. A General Method for Extracting Individual Coupling Constants from Crowded ^{1}H NMR Spectra. *Angew. Chem., Int. Ed.* **2016**, *55*, 1090–1093, DOI: 10.1002/anie.201508691.

Aguilar2018MRC   (54)   Aguilar, J. A.; Belda, R.; Gaunt, B. R.; Kenwright, A. M.; Kuprov, I. Separating the coherence transfer from chemical shift evolution in high-resolution pure shift COSY NMR. *Magn. Reson. Chem.* **2018**, *56*, 969–975, DOI: 10.1002/mrc.4727.

Kaltschnee2016JMR   (55)   Kaltschnee, L.; Knoll, K.; Schmidts, V.; Adams, R. W.; Nilsson, M.; Morris, G. A.; Thiele, C. M. Extraction of distance restraints from pure shift NOE experiments. *J. Magn. Reson.* **2016**, *271*, 99–109, DOI: 10.1016/j.jmr.2016.08.007.

Ilgen2021JMR   (56)   Ilgen, J.; Nowag, J.; Kaltschnee, L.; Schmidts, V.; Thiele, C. M. Gradient selected pure shift EASY-ROESY techniques facilitate the quantitative measurement of ^{1}H,^{1}H-distance restraints in congested spectral regions. *J. Magn. Reson.* **2021**, *324*, 106900, DOI: 10.1016/j.jmr.2020.106900.

Foroozandeh2016ACIE   (57)   Foroozandeh, M.; Castañar, L.; Martins, L. G.; Sinnaeve, D.; Poggetto, G. D.; Tormena, C. F.; Adams, R. W.; Morris, G. A.; Nilsson, M. Ultrahigh-Resolution Diffusion-Ordered Spectroscopy. *Angew. Chem. Int. Ed.* **2016**, *55*, 15579–15582, DOI: 10.1002/anie.201609676.

Frydman2002PNASUSA   (58)   Frydman, L.; Scherf, T.; Lupulescu, A. The acquisition of multidimensional NMR spectra within a single scan. *Proc. Natl. Acad. Sci. U. S. A.* **2002**, *99*, 15858–15862, DOI: 10.1073/pnas.252644399.

Pelupessy2003JACS   (59)   Pelupessy, P. Adiabatic Single Scan Two-Dimensional NMR Spectrocopy. *J. Am. Chem. Soc.* **2003**, *125*, 12345–12350, DOI: 10.1021/ja034958g.

Frydman2003JACS   (60)   Frydman, L.; Lupulescu, A.; Scherf, T. Principles and Features of Single-Scan Two-Dimensional NMR Spectroscopy. *J. Am. Chem. Soc.* **2003**, *125*, 9204–9217, DOI: 10.1021/ja030055b.

Kiraly2021ACIE   (61)   Kiraly, P.; Kern, N.; Plesniak, M. P.; Nilsson, M.; Procter, D. J.; Morris, G. A.; Adams, R. W. Single-Scan Selective Excitation of Individual NMR Signals in Overlapping Multiplets. *Angew. Chem., Int. Ed.* **2021**, *60*, 666–669, DOI: 10.1002/anie.202011642.

Dumez2018PNMRS   (62)   Dumez, J.-N. Spatial encoding and spatial selection methods in high-resolution NMR spectroscopy. *Prog. Nucl. Magn. Reson. Spectrosc.* **2018**, *109*, 101–134, DOI: `10.1016/j.pnmrs.2018.08.001`.

Nelder1965TCJ   (63)   Nelder, J. A.; Mead, R. A Simplex Method for Function Minimization. *The Computer Journal* **1965**, *7*, 308–313, DOI: `10.1093/comjnl/7.4.308`.

McKinnon1998SIAMJO   (64)   McKinnon, K. I. M. Convergence of the Nelder–Mead Simplex Method to a Nonstationary Point. *SIAM J. Optim.* **1998**, *9*, 148–158, DOI: `10.1137/s1052623496303482`.

Hogben2011JMR   (65)   Hogben, H. J.; Krzystyniak, M.; Charnock, G. T. P.; Hore, P. J.; Kuprov, I. Spinach – A software library for simulation of spin dynamics in large spin systems. *J. Magn. Reson.* **2011**, *208*, 179–194, DOI: `10.1016/j.jmr.2010.11.008`.

Khaneja2005JMR   (66)   Khaneja, N.; Reiss, T.; Kehlet, C.; Schulte-Herbrüggen, T.; Glaser, S. J. Optimal control of coupled spin dynamics: design of NMR pulse sequences by gradient ascent algorithms. *J. Magn. Reson.* **2005**, *172*, 296–305, DOI: `10.1016/j.jmr.2004.11.004`.

deFouquieres2011JMR   (67)   De Fouquieres, P.; Schirmer, S. G.; Glaser, S. J.; Kuprov, I. Second order gradient ascent pulse engineering. *J. Magn. Reson.* **2011**, *212*, 412–417, DOI: `10.1016/j.jmr.2011.07.023`.

Glaser2015EPJD   (68)   Glaser, S. J.; Boscain, U.; Calarco, T.; Koch, C. P.; Köckenberger, W.; Kosloff, R.; Kuprov, I.; Luy, B.; Schirmer, S.; Schulte-Herbrüggen, T.; Sugny, D.; Wilhelm, F. K. Training Schrödinger's cat: quantum optimal control. *Eur. Phys. J. D* **2015**, *69*, No. 279, DOI: `10.1140/epjd/e2015-60464-1`.

Goodwin2016JCP   (69)   Goodwin, D. L.; Kuprov, I. Modified Newton-Raphson GRAPE methods for optimal control of spin systems. *J. Chem. Phys.* **2016**, *144*, 204107, DOI: `10.1063/1.4949534`.

Geen1989JMR   (70)   Geen, H.; Wimperis, S.; Freeman, R. Band-selective pulses without phase distortion. A simulated annealing approach. *J. Magn. Reson.* **1989**, *85*, 620–627, DOI: `10.1016/0022-2364(89)90254-0`.

Geen1991JMR   (71)   Geen, H.; Freeman, R. Band-selective radiofrequency pulses. *J. Magn. Reson.* **1991**, *93*, 93–141, DOI: `10.1016/0022-2364(91)90034-q`.

Nuzillard1994JMRSA   (72)   Nuzillard, J. M.; Freeman, R. Band-Selective Pulses Designed to Accommodate Relaxation. *J. Magn. Reson., Ser. A* **1994**, *107*, 113–118, DOI: `10.1006/jmra.1994.1056`.

Kupce1995JMRSA   (73)   Kupce, E.; Freeman, R. Band-Selective Correlation Spectroscopy. *J. Magn. Reson., Ser. A* **1995**, *112*, 134–137, DOI: `10.1006/jmra.1995.1023`.

Emsley1990CPL   (74)   Emsley, L.; Bodenhausen, G. Gaussian pulse cascades: New analytical functions for rectangular selective inversion and in-phase excitation in NMR. *Chem. Phys. Lett.* **1990**, *165*, 469–476, DOI: `10.1016/0009-2614(90)87025-m`.

Ewing1990CP   (75)   Ewing, B.; Glaser, S. J.; Drobny, G. P. Development and optimization of shaped NMR pulses for the study of coupled spin systems. *Chem. Phys.* **1990**, *147*, 121–129, DOI: `10.1016/0301-0104(90)85028-u`.

Verstraete2022JMR (76) Verstraete, J.-B.; Foroozandeh, M. Improved design of frequency-swept pulse sequences. *J. Magn. Reson.* **2022**, *336*, 107146, DOI: 10.1016/j.jmr.2022.107146.

Higham2005SIAMJMAA (77) Higham, N. J. The Scaling and Squaring Method for the Matrix Exponential Revisited. *SIAM J. Matrix Anal. Appl.* **2005**, *26*, 1179–1193, DOI: 10.1137/04061101x.

Moler2003SIAMR (78) Moler, C.; Van Loan, C. Nineteen Dubious Ways to Compute the Exponential of a Matrix, Twenty-Five Years Later. *SIAM Rev.* **2003**, *45*, 3–49, DOI: 10.1137/s00361445024180.

Kelley1999 (79) Kelley, C. T., *Iterative Methods for Optimization*; Society for Industrial and Applied Mathematics: 1999, DOI: 10.1137/1.9781611970920.

Nocedal2006 (80) Nocedal, J.; Wright, S. J., *Numerical Optimization*, 2nd ed.; Springer: New York, 2006.

Johnson1999PNMRS (81) Johnson Jr., C. S. Diffusion ordered nuclear magnetic resonance spectroscopy: principles and applications. *Prog. Nucl. Magn. Reson. Spectrosc.* **1999**, *34*, 203–256, DOI: 10.1016/s0079-6565(99)00003-5.

Stejskal1965JCP (82) Stejskal, E. O.; Tanner, J. E. Spin Diffusion Measurements: Spin Echoes in the Presence of a Time-Dependent Field Gradient. *J. Chem. Phys.* **1965**, *42*, 288–292, DOI: 10.1063/1.1695690.

Sinnaeve2012CMR (83) Sinnaeve, D. The Stejskal–Tanner equation generalized for any gradient shape—an overview of most pulse sequences measuring free diffusion. *Concepts Magn. Reson.* **2012**, *40A*, 39–65, DOI: 10.1002/cmr.a.21223.

Wu1996JMRSA (84) Wu, D.; Chen, A.; Johnson Jr., C. S. Three-Dimensional Diffusion-Ordered NMR Spectroscopy: The Homonuclear COSY–DOSY Experiment. *J. Magn. Reson., Ser. A* **1996**, *121*, 88–91, DOI: 10.1006/jmra.1996.0142.

Jerschow1996JMRSA (85) Jerschow, A.; Müller, N. 3D Diffusion-Ordered TOCSY for Slowly Diffusing Molecules. *J. Magn. Reson., Ser. A* **1996**, *123*, 222–225, DOI: 10.1006/jmra.1996.0241.

Vitorge2006AC (86) Vitorge, B.; Jeannerat, D. NMR Diffusion Measurements in Complex Mixtures Using Constant-Time-HSQC-IDOSY and Computer-Optimized Spectral Aliasing for High Resolution in the Carbon Dimension. *Anal. Chem.* **2006**, *78*, 5601–5606, DOI: 10.1021/ac060744g.

McLachlan2009MRC (87) McLachlan, A. S.; Richards, J. J.; Bilia, A. R.; Morris, G. A. Constant time gradient HSQC-iDOSY: practical aspects. *Magn. Reson. Chem.* **2009**, *47*, 1081–1085, DOI: 10.1002/mrc.2518.

PereaBuceta2021JMR (88) Perea-Buceta, J.; Rico del Cerro, D.; Kilpeläinen, I.; Heikkinen, S. Incorporated diffusion ordered heteronuclear multiple bond correlation spectroscopy, 3D iDOSY-HMBC. Merging of diffusion delay with long polarization transfer delay of HMBC. *J. Magn. Reson.* **2021**, *323*, 106892, DOI: 10.1016/j.jmr.2020.106892.

Cobas2004JMR (89) Cobas, J. C.; Martín-Pastor, M. A homodecoupled diffusion experiment for the analysis of complex mixtures by NMR. *J. Magn. Reson.* **2004**, *171*, 20–24, DOI: 10.1016/j.jmr.2004.07.016.

Nilsson2007CC (90) Nilsson, M.; Morris, G. A. Pure shift proton DOSY: diffusion-ordered ^{1}H spectra without multiplet structure. *Chem. Commun.* **2007**, 933, DOI: 10.1039/b617761a.

Glanzer2014CEJ (91) Glanzer, S.; Zangger, K. Directly Decoupled Diffusion-Ordered NMR Spectroscopy for the Analysis of Compound Mixtures. *Chem. Eur. J.* **2014**, *20*, 11171–11175, DOI: 10.1002/chem.201402920.

Telkki2021PNMRS (92) Telkki, V.-V.; Urbańczyk, M.; Zhivonitko, V. Ultrafast methods for relaxation and diffusion. *Prog. Nucl. Magn. Reson. Spectrosc.* **2021**, *126-127*, 101–120, DOI: 10.1016/j.pnmrs.2021.07.001.

Loening2001JMR (93) Loening, N. M.; Keeler, J.; Morris, G. A. One-Dimensional DOSY. *J. Magn. Reson.* **2001**, *153*, 103–112, DOI: 10.1006/jmre.2001.2423.

Thrippleton2003MRC (94) Thrippleton, M. J.; Loening, N. M.; Keeler, J. A fast method for the measurement of diffusion coefficients: one-dimensional DOSY. *Magn. Reson. Chem.* **2003**, *41*, 441–447, DOI: 10.1002/mrc.1195.

Shrot2008JMR (95) Shrot, Y.; Frydman, L. Single-scan 2D DOSY NMR spectroscopy. *J. Magn. Reson.* **2008**, *195*, 226–231, DOI: 10.1016/j.jmr.2008.09.011.

Guduff2017CC (96) Guduff, L.; Kuprov, I.; van Heijenoort, C.; Dumez, J.-N. Spatially encoded 2D and 3D diffusion-ordered NMR spectroscopy. *Chem. Commun.* **2017**, *53*, 701–704, DOI: 10.1039/c6cc09028a.

Jacquemmoz2022MRC (97) Jacquemmoz, C.; Mishra, R.; Guduff, L.; Heijenoort, C.; Dumez, J.-N. Optimisation of spatially-encoded diffusion-ordered NMR spectroscopy for the analysis of mixtures. *Magn. Reson. Chem.* **2022**, *60*, 121–138, DOI: 10.1002/mrc.5194.

Mansfield1977JPCSSP (98) Mansfield, P. Multi-planar image formation using NMR spin echoes. *J. Phys. C: Solid State Phys.* **1977**, *10*, L55–L58, DOI: 10.1088/0022-3719/10/3/004.

Stehling1991S (99) Stehling, M.; Turner, R.; Mansfield, P. Echo-planar imaging: magnetic resonance imaging in a fraction of a second. *Science* **1991**, *254*, 43–50, DOI: 10.1126/science.1925560.

Tal2010PNMRS (100) Tal, A.; Frydman, L. Single-scan multidimensional magnetic resonance. *Prog. Nucl. Magn. Reson. Spectrosc.* **2010**, *57*, 241–292, DOI: 10.1016/j.pnmrs.2010.04.001.

Giraudeau2014ARAC (101) Giraudeau, P.; Frydman, L. Ultrafast 2D NMR: An Emerging Tool in Analytical Spectroscopy. *Annu. Rev. Anal. Chem.* **2014**, *7*, 129–161, DOI: 10.1146/annurev-anchem-071213-020208.

Gouilleux2018ARNMRS (102) Gouilleux, B.; Rouger, L.; Giraudeau, P. Ultrafast 2D NMR: Methods and Applications. *Annu. Rep. NMR Spectrosc.* **2018**, 75–144, DOI: 10.1016/bs.arnmr.2017.08.003.

refsection:3

refsection:4

refsection:5